

Supplemental data

Methods

Primary samples

Normal donor blood was obtained from Research Blood Components, LLC; and mononuclear cells (PBMCs) were isolated using Ficoll-Paque PLUS from GE Healthcare. Ayala Pharmaceuticals is currently investigating AL101 (BMS-906024) in a Phase II open-label, single-arm, multicenter study in ACC patients harboring known *NOTCH1-4* activating mutations (ACCURACY; NCT03691207).

In vitro inhibitor and cell proliferation assays

Cell proliferation was measured by CellTiter-Glo (Promega). Buparlisib (Selleckchem) and GSI (Santa Cruz Biotechnology, Inc) were prepared in DMSO (Sigma-Aldrich). IC50 values were calculated by fitting the dose-response curves to a three-parameter sigmoid dose-response model using GraphPad. Error bars reflect standard deviation. Synergy of combination treatment was calculated using CompuSyn (ComboSyn Inc., Paramus, NJ)¹. Single cells were treated for 72h with 1 μ M Buparlisib or DMSO control then sorted into 96-well round bottom plates and continuously cultured with 1 μ M GSI (Compound E) or DMSO control. The number of clones that grew after 6 weeks of culture was determined using a Nikon eclipse TS100 ELWD 0.3/OD75 with a 20x objective imaging system. A total of 480 wells were analyzed per condition.

Flow cytometry

Primary and PDX samples were stained with anti-CD45-FITC and DAPI, primary samples were also stained with anti-CD3-PerCP-Cy5.5 (Thermo Fisher Scientific), anti-CD14-APC-Cy7 (BD Biosciences), and anti-CD19-PE (BioLegend). Single cells were sorted into 96-well plates containing TCL buffer (Qiagen) using a Sony SH800 sorter (Figures S23, S24). Other antibodies used were anti-Galectin-9-APC (BioLegend), anti-phospho-4E-BP1 (Ser65) (Cell Signaling), anti-phospho-AKT (Thr308) (BD Biosciences), or isotype control Mouse IgG1, κ (Thermo Fisher Scientific). Stained cells were analyzed on a BD LSRFortessa flow cytometer (BD) using FlowJo software v10.

Targeted Sequencing

DNA was extracted using DNeasy Blood and Tissue Kit (Qiagen) according to the manufacturer's protocol. The panel of targeted genes with known mutations was designed according to previous publications². 10ng of input DNA was used to amplify amplicons using KAPA HiFi HotStart ReadyMix PCR kit (Roche). PCR bands were purified using MinElute PCR purification according to manufacturer's protocol (Qiagen). Bands were pooled at equimolar concentration, following library preparation. Products were quantified using Agilent High Sensitivity D5000, TapeStation Systems (Agilent). Pooled libraries were sequenced on a NextSeq 500 instrument (Illumina).

Processing of scRNA-seq data

Sequencing reads were trimmed using trimmomatic and aligned to the hg19 version of the genome using STAR aligner with following parameters '`--twopassMode Basic --alignIntronMax 100000 --alignMatesGapMax 100000 --alignSJDBoverhangMin 10 --alignSJstitchMismatchNmax 5 - 1 5 5`'^{3,4}. Raw counts and normalized TPM values were obtained from the aligned bam file using HTSeq and RSEM, respectively^{5,6}.

Quality filtering of scRNA-seq data

In order to filter out low quality cells from our dataset, we used four different parameters – i) library size, ii) number of genes detected, iii) percentage of reads mapping to mitochondrial genes, and iv) percentage of reads mapping to house-keeping genes (Figure S1A). Cells in the distribution that were beyond three median absolute deviations (M.A.D's) were flagged as low quality cells. Poor quality cells were also identified without any predefined cut-offs using the R package '*mvoutlier*' (Figure S1B). Cells that were detected as outliers by both MAD-based cut-offs and *mvoutlier* predictions were filtered out from the dataset (Figure S1C). This resulted in retention of 3562 high-quality cells for further downstream analyses (Figure S1D). On average 3,330 genes were detected in these cells (Figure S1E). The variance in the dataset was also used to systematically investigate the contribution of various technical factors and batch effects. The proportion of variance explained by the variables such as – individual patients, total number of genes detected, sequencing run and library size were found to be low (Figure S1F). Similar quality filtering thresholds were applied to the T-ALL and the ETP-ALL PDXs (1,118 of high-quality cells, average of 4,463 genes per cell).

Clustering of scRNA-seq profiles and identification of cell-types

Clustering of high-quality cells was performed using PAGODA2⁷. In order to rule out the possibility of clusters being purely driven by cell-cycle, each individual cell was analyzed for expression of G1, G2M and S phase markers to predict the cell-cycle phase using Seurat2⁸. The observed clusters did not show high concordance with the cell-cycle stages as indicated by low adjusted-rand index (0.0207; as calculated by *adjustedRandIndex* function of *mclust* package in R), thus ruling out the possibility of cell-cycle being a major contributor to differences between clusters. The marker genes for each of the clusters were determined using *findMarker* function in the *scrna* package⁹. Using the information of the marker genes, the individual clusters consisting of normal cells were manually annotated to be either CD4⁺ T-cells, CD8⁺ T-cells, NK cells, myeloid or B-cells (Figure 1).

Identification of pathogenic variants from scRNA-seq data

The workflow for detecting SNVs was adapted from GATK best practices¹⁰. In brief, the aligned reads in BAM format were sorted, duplicate reads were flagged, read filters applied, (*SplitNCigarReads*, GATK 4.0), local realignment performed to minimize the number of mismatching bases across all reads (*RealignerTargetCreator* and *IndelRealigner*, GATK 4.0), base scores were recalibrated (*BaseRecalibrator*, GATK 4.0), and finally *mutect2*¹¹ was used for variant calling and *oncotator* for annotation of called mutations¹². All of the mutations in expressed genes with allele frequencies > 40% were detected, except for JAK1 p.S703I in patient 3, which was only supported by 16 reads in *RapidHemePanel* (Table 1).

Detection of copy number variations from scRNA-seq and cytogenetics

The copy number variants were inferred from the scRNA-seq data using *InferCNV*^{13,14} (<https://github.com/broadinstitute/inferCNV>) and *CONICSmat*¹⁵ (<https://github.com/diazlab/CONICS>). Binarized calls from *CONICS* ($p \geq 0.065$) at single-cell level were used to call the CNVs and each of the CNV calls at the chromosome-arm level were visually confirmed from the heatmap output of *inferCNV*. T-cells from the normal donors were used as controls for both methods. The detected CNVs were compared to the cytogenetics report obtained as clinical routine

(Table 1). The signals for copy-number variations through inferCNV could detect duplication of chr21 that was in agreement for P1 and del7p for P2. The deletion of 1p, 4q, 6q and 11q could be reliably identified for P4 and del12p was specifically predicted for P5. No strong signals for copy number variations could be identified from scRNA-seq for P3. In addition to these, we also could capture additional copy number signals that were not reported by cytogenetics such as amp10q, del4q for P1, amp9q for P2, del9p for P4 (Figure S5).

Comparison to bulk RNA-seq from ImmGen and BLUEPRINT datasets

The expression data from the purely sorted bulk populations of immune cells from the ImmGen¹⁶ and BLUEPRINT¹⁷ datasets were used to define the identity of cell types. We used a multinomial log-likelihood model reported by Zemmour et al.¹⁸ to determine the probability of each cell belonging to a particular cell type. The bulk RNA-seq gene expression matrix was used to provide prior probabilities (probability to express gene i in cell-type $j = p_{ij}$), and for each cell c we calculated the likelihood of it belonging to cell-type j (L_{cj}). For normalization, the log posterior probabilities were summed to one during calculation.

$$L_{cj} = \sum_i c_i \times \log(p_{ij})$$

Evaluating relative importance of transcription factors using random-forest model

We employed a random-forest model in order to evaluate the relative importance of transcription factors in distinguishing between malignant and non-malignant cells. The relative expression of all the transcription factors from the transcription factor database Animal TFDB¹⁹ were used as features. The cells belonging to patient-specific clusters, having specific enrichment for pathogenic variants and copy-number aberrations were defined as malignant. A random-forest classifier²⁰ was built in R using this definition of malignant and non-malignant as labels. Around 70% of the data was used to build the model. The optimum parameters – *mtry* (39) and *ntrees* (400) for randomforest were determined using *tuneRF* function. The best model had the OOB estimate of error rate at 2.65% with 0.049 and 0.005 % class error rate. The relative importance of transcription factors in classification was evaluated using *varImpPlot* function. The process was repeated by both including and excluding the GSI treated cells.

Determining the co-existing/mutually exclusive signatures in malignant cells

The signatures for the hematopoietic stem cells (HSCs), multipotent-progenitors (MPP), common lymphoid progenitors (CLP), common myeloid progenitor (CMP) and granulocyte-macrophage progenitors (GMP) were derived from previously published literature comprising bulk RNA-seq studies on purely sorted immune populations^{17,21}. The genes in each of these signatures were scored using AUCCell package²². All the malignant cells were observed to have high scores for HSC-program. Few of these malignant cells were also observed to have high CLP-program score, but more often also had high scores for other programs such as CMP, GMP and MPP within the same malignant cell. The pre-thymic gene signatures were derived from ImmGen portal¹⁶. The population comparison app was used to identify the differentially expressed genes at specific stage of thymic maturation by systematically comparing the pre- and post-stages, focusing on early T-cell progenitor (ETP), double-negative 1 (DN1), double-negative 2 (DN2), double-negative 2-3 (DN2-3), double-negative 3A (DN3A), double-negative 3B (DN3B), double-negative 3-4 (DN3-4), double-negative 4 (DN4) and double-positive (DP). For example, in order to specifically determine the gene signature associated with ‘DN2A’, the genes had to be upregulated in ‘DN2A’ in comparison to earlier DN1 stage and the later DN2B population as well. In order to determine

the promiscuity of various programs in malignant cells, we analyzed the human cell atlas (<https://preview.data.humancellatlas.org/>) consisting of 335,618 cells from bone marrow of eight different donors using scanpy²³. Louvain clustering of the single-cell profiles revealed 21 different clusters in human immune cell atlas. The same genes signatures were used to score the normal cells using scanpy.api.tl.score_genes function within scanpy. Clusters 8, 9 and 13 were observed to have high scores for the HSC-program, CMP-program and CLP-program, respectively. These signatures were further refined by obtaining the marker genes for cluster 8, 9 and 13 of the human cell atlas. The scatterplot using these signatures revealed a mutually exclusive pattern with negative correlation in normal condition at single-cell resolution. The trend was reversed with positive correlation between these signatures observed in malignant cells confirming the promiscuity of the gene expression programs.

Characterization of heterogeneity at single cell resolution

Monocle2 was employed to discover the subclusters within each of the patient-specific T-ALL cell clusters using only the raw counts from single cells²⁴. The clusters derived using this approach for P2 and P4 overlapped with the clusters derived from graph-based infomap clustering algorithm applied on RNA velocity²⁵. Finally, a perturbation-response based score for assessing the signaling activity in each cell²⁶ was also used to characterize the heterogeneous clusters.

Defining TCR-usage in CD8⁺ T-cells

We defined TCR usage group has previously described¹⁴ by considering the frequency of the read counts aligned to the V and the J locus of the alpha and the beta chains (V_{α} , J_{α} , V_{β} and J_{β}). The sequences of different alleles for TCRs were downloaded from the IMGT database and aligned using ncbi-magicblast²⁷. Each cell was assigned V and J allele for alpha and beta TCR chain based on the number of reads uniquely aligned. Two cells were considered to belong to same clonotype if three of the four alleles overlapped.

Exhaustion score and receptor-ligand interaction scores

T-cell exhaustion, naïve and cytotoxic scores were calculated by average relative expression of key marker genes from the literature¹⁴. The exhaustion score was defined as difference between average relative expression of exhaustion markers – *PDCDI*, *TIGIT*, *LAG3*, *HAVCR2*, *CTLA4* and naïve markers – *CCR7*, *TCF7*, *LEF1* and *SELL*. The cytotoxic score was defined as difference between average relative expression of cytotoxic markers – *NKG7*, *CCL4*, *CST7*, *PRF1*, *GZMA*, *GZMB*, *IFNG*, *CCL3* and naïve markers. The co-inhibitory ligand and receptor pairs that could potentially result in exhaustion were derived from reviewed literature²⁸. The ligand-receptor pairs were scored based on their expression levels as described²⁹.

Supplementary Figure Legends

Figure S1. Quality filtering of scRNA-seq dataset. (A) Distribution of features in the unfiltered dataset – (i) library size per cell, (ii) number of genes detected in each cell, (iii) percentage of counts mapping to mitochondrial genes in each cell and (iv) percentage of counts mapping to house-keeping genes (HKG) in all cells sequenced. (B) Scatter plot depicting the result of principal component analyses using the top two dimensions. The PCA was performed on these four features for all the 5,077 cells. The outliers were detected using mvoutlier package and are highlighted in

orange. (C) Venn diagram depicting the overlap between the outliers detected by mvoutlier (blue) and manual cut-offs (red) using median absolute deviations (M.A.D's). (D) Distribution of the features after filtering out the cells detected to be outlier by both the methods. (E) Scatter plot depicting the quality of data from the remaining 3,562 cells through expression frequency and mean read counts per gene. (F) Density plot depicting the contribution of various technical factors contributing to the total variation observed in entire dataset.

Figure S2. Confirming the identity of non-malignant immune cell clusters. (A) Heatmap depicting the log-likelihood scores derived by comparison of scRNA-seq profile to the bulk RNA-seq profile obtained from purely sorted immune populations. These bulk RNA-seq profiles were obtained from BLUEPRINT. The identity of the non-malignant clusters was further validated by confirming the expression of the specific marker genes of these clusters in all the immune cell-types from ImmGen consortium. Marker genes obtained for (B) cluster 1 show specific expression in CD8⁺ T-cells; (C) cluster 7 show specific expression in the NK cell population; (D) cluster 8 show specific expression in the B-cell population; (E) cluster 10 show specific expression in CD4⁺ T-cell population and (F) cluster 11 show specific expression in the myeloid population from ImmGen dataset.

Figure S3. Effect of cell-cycle on clustering of scRNA-seq data. (A) PCA plot derived by considering all the genes involved in cell-cycle using SEURAT. (B) t-SNE plot of scRNA-seq profiles. Each dot represents a cell and is colored based on the cell-cycle phase predicted by SEURAT. (C) Scatterplot depicts G2M and S-score obtained for each of the cells. Cells are colored based on the clusters obtained from PAGODA2. (D) Stacked bar plot depicting the relative distribution of different cell-cycle phases in each of the clusters. Notably, the malignant clusters from patients tend to have a greater fraction of cells in S and G2M phase.

Figure S4. Distribution of normal donor cells and pathogenic SNVs. (A) Distribution of normal T-cells from four different normal donors. (B) Distribution of different pathogenic variants detected using CLIA-certified next-generation sequencing panel (RHP) and confirmed through scRNA-seq profiling using Mutect2. P1: *ETV6*_p.R369Q, *ETV6*_p.R369W, *NOTCH1*_p.Q2391*, (C) P2: *CSF3R*_p.T618I, *NOTCH1*_p.F1592C, *DNMT3A*_p.Q402*, (D) P3: *IL7R*_p.I241N, *GATA3*_p.R276Q, *NOTCH1*_p.R1598P, (E) P4: *NOTCH1*_p.L1574P, (F) P5: *JAK3*_p.E958K, *JAK1*_p.R724H, *NOTCH1*_p.L1593P.

Figure S5. Copy number variation (CNV) profile from scRNA-seq data. (A) Profile depicting the amplifications and deletion signals from all patients' cells using inferCNV. T-cells from healthy donors (top panel) were used as control. (B) The Gaussian mixture model (GMM) fit to distinguish between malignant and non-malignant cells by using CONICSMAT algorithm. The model fit for five CNV events depicted in Figure 1 is shown here.

Figure S6. Known T-ALL transcription factor expression in ETP-ALL patients. t-SNE plot depicting expression of various transcription factors known to be generally deregulated in T-ALL. All five leukemias show expression of LMO2 and LYL1 transcription factors. A subset of leukemias also expresses TAL1 and HOX transcription factors.

Figure S7. Comparison to T-ALL subtypes identified in TARGET study. (A) t-SNE plot colored based on the T-ALL classification obtained from the TARGET study³⁰. Each dot represents the bulk-RNA seq profile from individual patient. (B) same t-SNE plot as in (A), colored based on the clusters derived from SC3 tool. (C) Silhouette plot depicting the confidence of each of the clusters obtained. (D) The data from single cell sequencing were collapsed for individual ETP-ALL patients. All five patients in the study had five 96-well SMART-seq2 plates sequenced. The sequencing reads from each of the plates were collapsed, hence five replicates were obtained for each patient. Each of these replicates were compared to average expression profile of individual T-ALL subtype clusters to obtain the log-likelihood score. The x-axis depicts the T-ALL subtypes along with corresponding sc3 cluster. The similarity of collapsed patient-specific data to the expression profile of each T-ALL subtype is depicted on y-axis (log-likelihood). All patients showed high similarity to ETP-ALL subtype with deregulated expression of LMO2-LYL1. Only patient P3 showed high transcriptional similarity to TLX3 subtype of T-ALL in 3/5 replicates.

Figure S8. Random forest model trained on transcription factors. (A) Plot depicting the relationship between the error and number of trees used by random forest model on malignant (green), non-malignant (red) and combined (black) by considering all the malignant and non-malignant cells sequenced. The relative importance of each of the transcription factors in the model is depicted below. (B) the same plots as (A), generated by training the model only on the untreated cell population.

Figure S9. Random Forest ranked transcription factor expression in normal hematopoietic progenitors and thymocytes. Heatmap demonstrates expression of highly ranked transcription factors (*SOX4*, *BCL11A*, *NFE2*, *NOTCH1*, *MYB*, *ERG*, *ETV6*, *TFDP2*, *KDM5B*, *ZMIZ1*) in SC_LTSL_BM (long-term repopulating hematopoietic stem cell), SC_STSL_BM (short-term repopulating hematopoietic stem cell), SC_LTSL_FL (long-term reconstituting stem cell, SLAM series), SC_STSL_FL (short-term reconstituting stem cell, SLAM series), SC_MPP34F_BM (multipotent progenitor), SC_ST34F_BM (multipotent progenitor), SC_CMP_BM_DR (common myeloid progenitor), SC_MEP_BM (megakaryocyte-erythroid progenitor), SC_GMP_BM (granulocyte-monocyte progenitor), SC_CDP_BM (common DC precursors (CDP)), SC_MDP_BM (monocyte DC precursors (MDP)), MLP_BM (multilineage progenitor), MLP_FL (multilineage progenitor), proB_CLP_BM (common lymphoid progenitor), proB_CLP_FL (common lymphoid progenitor), proB_FrA_BM (Fr. A (pre-pro-B)), proB_FrA_FL (Fr. A (pre-pro-B)), proB_FrBC_BM (proB.FrBC.BM), proB_FrBC_FL (Fr. B/C (pro-B)), preB,FrC_BM (Fr. Cprime (cycling pre-B)), preB_FrD_BM (small pre-B population, Fr.D), preB_FrD_FL (Fr D (pre-B)), preT_ETP_Th (Early T lineage precursor), preT_ETP-2A_Th (ETP to DN2a transitional), preT_DN2_Th (double negative 2 thymocytes), preT_DN2A_Th (double negative 2A thymocytes), preT_DN2B_Th (double negative 2B thymocytes), preT_DN2-3_Th (DN2 to DN3 transitional), preT_DN3A_Th (double negative 3A thymocytes), preT_DN3B_Th (double negative 3B thymocytes), preT_DN3-4_Th (DN3 to DN4 transitional), T_DN4_Th (double negative 4 thymocytes), T_4Nve_Sp (spleen naïve CD4), T_4Mem_Sp (spleen memory-phenotype CD4), T_8Nve_sp (spleen naïve CD8) and T_8Mem_Sp (spleen memory-phenotype CD8) profiled by ImmGen¹⁶.

Figure S10. Random Forest ranked transcription factor expression in cancer cell lines. Expression of random forest ranked transcription factors in cancer cell lines profiled by CCLE³¹.

Arrow indicates T-ALL cell lines. (A) *SOX4*, (B) *ERG*, (C) *MYB*, (D) *NFE2*, (E) *BCL11A*, (F) *ETV6*, (G) *ZMIZ1*, (H) *TFDP2*, (I) *KDM5B*, (J) *NOTCH1*.

Figure S11. Expression of random forest ranked transcription factors in BLUEPRINT and TARGET. Expression of *SOX4*, *ERG*, *MYB*, *NFE2*, *BCL11A*, *ETV6*, *ZMIZ1*, *TFDP2*, *KDM5B*, *NOTCH1* and *CD34* in (A) different types of human hematopoietic and immune cells from BLUEPRINT¹⁷ and (B) National Cancer Institute TARGET study of T-ALL³⁰.

Figure S12. Deranged developmental hierarchy with ineffectual commitment in ETP-ALL compared to normal bone marrow cells. (A) Expression of HSC, CMP and CLP signatures in single normal bone marrow cells from the human cell atlas (top), and ETP-ALL cells (bottom) demonstrating lineage promiscuity in leukemic cells compared to normal BM cells (see methods). (B) Expression of HSC, CMP and CLP signatures in single human thymocytes and mature T-cells as profiled by the thymic human cell atlas³².

Figure S13. Distribution of co-existing root and endpoint cells in ETP-ALL. RNA-velocity distribution of cells (%) in root or endpoint states across different Louvain clusters depicted as stacked bar plot.

Figure S14. GSI treatment and its effect on cell-cycle, Notch target genes and oncogenic signaling in leukemic cells. (A) t-SNE plot with treated leukemic cells colored according to days of GSI treatment. (B) Scatter plot depicting the G2M and S-phase scores for all the leukemic cells in root 1, root 2 and endpoint states. (C), (D), (E) Stacked barplots depicting the relative distribution of different phases of cell cycle with treatment in patients P3, P4 and P5. (F) Heatmap depicting the downregulation of Notch targets upon GSI treatment in patient P5. (G) Subclusters identified in each of the patient-specific leukemic clusters using monocle2 are depicted on t-SNE. (H) Violin plot depicting the PI3K activity score inferred by average relative expression of PI3K targets as inferred by PROGEny upon GSI treatment in all patients.

Figure S15. Co-existing root states with PI3K and Notch activation signatures in ETP and T-ALL PDX samples. Deconvolution of distinct stem-like state signatures using CIBERSORT in ETP (A) and T-ALL (G) PDX samples. t-SNE plots using genes involved in HSC, CLP and CMP progenitor programs, colored by PDX model (ETP, B), (T-ALL, H) and clusters as identified by Louvain algorithm in ETP (C), and T-ALL PDXs (I). RNA velocity projections onto t-SNE identifying two root and endpoint states in ETP (D) and T-ALL PDXs. (J) t-SNE plots colored by cell cycle phase in ETP (E) and T-ALL PDXs (K). Correlation plots of relative Notch and PI3K activity in ETP (F) and T-ALL PDXs (L), based on *NOTCH1* mutation and *PTEN* deletion status. * = *NOTCH1* mutation, # = *PTEN* deletion.

Figure S16. Deconvolution of root and endpoint signatures in bulk T-ALL RNA-seq data. (A) Relative fractions of root 1, root 2 and endpoint expression signatures after deconvolution ordered by endpoint fraction using CIBERSORT in bulk RNA-seq data from TARGET cohort. (B) Relative fractions of root 1, root 2 and endpoint expression signatures in T-ALL subtypes in TARGET cohort.

Figure S17. Correlation plots of signaling pathways in root 1 and root 2 ETP-ALL cells.

(A) EGFR, (B) Hypoxia, (C) JAK-STAT, (D) MAPK, (E) NF κ B, (F) PI3K, (G) TGF β (H) TNF α , (I) Trail, (J) p53, (K) MYC, and (L) PIM.

Figure S18. Inferred signaling pathway activity in single cells of each patient before and after GSI treatment. Heatmaps depict the relative activity of various signaling pathways as inferred by PROGENy and signatures for Notch, PIM and MYC, before and after treatment, cell cycle phase and root and endpoint status. (A) Patient 1, (B) Patient 2, (C) Patient 3, (D) Patient 4, (E) Patient 5.

Figure S19. Inhibition of T-ALL proliferation by PI3K inhibitor is increased when combined with GSI. DND-41, HPB-ALL and Jurkat T-ALL cell lines were treated with Buparlisib and GSI alone or in combinations of 1 μ M Buparlisib with 1 μ M of GSI or 0.25 μ M Buparlisib with 1 μ M of GSI, respectively, for 7 days. Dose response curves of cell viability normalized to DMSO (datapoints are derived from 3 replicates each, error bars show standard deviation) and corresponding synergy analyses are shown. (A) DND-41: IC₅₀ = 1.01 μ M for Buparlisib, 0.132 μ M for Buparlisib and GSI. (B) HPB-ALL: IC₅₀ = 0.34 μ M for Buparlisib, 7.23e-006 μ M for Buparlisib and GSI. (C) Jurkat: IC₅₀ = 0.72 μ M for Buparlisib, 0.423 μ M for Buparlisib and GSI. (D) Flow cytometry demonstrating subpopulation of CD34⁺ population staining positive for p4E-BP1 (S65) and pAKT (Thr308) in DND-41 cells (overlay histogram gated on CD34⁺ or CD34⁻ cells, respectively).

Figure S20. Inhibitory receptor-ligand interactions. (A) t-SNE plots depicting the expression of various inhibitory receptors and corresponding ligands on exhausted T-cells and T-ALL cells. (B) Violin plot depicts the expression of LGALS9 across T-ALL subsets from TARGET study.

Figure S21. LGALS9 protein expression in T-ALL leukemia cell lines determined by flow cytometry. Intracellular LGALS9 fluorescence (dark gray) compared to mouse IgG1, κ (light gray) shown as histograms. (A) T-ALL cell lines, HPB-ALL, KOPT-K1, Loucy and MOLT-4. (B) B-ALL cell lines, NALM-6 and SEM. (C) AML cell lines, KG-1 and HL-60.

Figure S22. Blockade of LGALS9 with neutralizing antibody inhibits HAVCR2 expression. *HAVCR2* mRNA expression in activated CD8⁺ T-cells cultured with T-ALL supernatant (from DND-41 cells; orange) or control media (blue), in the presence/absence of anti-human Galectin-9 (10 μ g/mL) or recombinant Galectin-9 (2.5 μ g/mL). n.s. P>0.05, ** P \leq 0.01 and *** P \leq 0.001, based on 3 technical replicates, using two-sided t-test, error bars reflect standard deviation.

Figure S23. Flow cytometry gating strategy of T-ALL leukemic blasts. ETP-ALL samples were stained with anti-CD45 FITC and DAPI. CD45^{low} expressing, DAPI negative single cells were sorted.

Figure S24. Flow cytometry gating strategy of normal immune cells. PBMCs were stained with DAPI, anti-CD45 FITC, anti-CD3 PerCP-Cy5.5, anti-CD19 PE, anti-CD14 APC-Cy7. CD45^{high} CD3⁺ DAPI negative (T-cells), CD45^{high} CD19⁺ DAPI negative (B-cells), CD45^{high} CD14⁺ DAPI negative (monocytes) single cells were sorted.

Supplementary Table Legends

Table S1: Primer sequences used for qRT-PCR and targeted sequencing.

Table S2: Differential marker gene analysis for malignant clusters derived from PAGODA/t-SNE analysis.

Table S3: Number of cells per patient and cluster (PAGODA).

Table S4: Differential marker gene analysis for patient 1 compared to high cycling leukemia cells from cluster 9.

Table S5: Differential marker gene analysis for patient 3 compared to high cycling leukemia cells from cluster 9.

Table S6: Differential marker gene analysis for patient 5 compared to high cycling leukemia cells from cluster 9.

Table S7: Differential marker gene analysis for high cycling leukemia cells from cluster 9 compared to the remaining malignant clusters.

Table S8: List of mutation calls detected in single cells using Mutect2 and filtered for patient specific SNVs.

Table S9: List of copy number variants (CNV) detected in single cells using CONICS for amplifications of chromosomes 6p, 9p, 12p, 13q, 19p, 22q and deletions of 7p, 9q, 10q, 21q; filtered for patient specific SNVs. (1=detected, 0=not detected, N/A= not covered).

Table S10: Differential marker gene analyses in root 1 and root 2 cells.

Table S11: Differential marker gene analysis in endpoint cells.

Table S12: Results of GSEA analyses performed on ranked gene lists from root cells in comparison to endpoint cells by using the hallmark gene sets (H), curated gene sets (C2), oncogenic gene sets (C6) and immunologic gene sets (C7) signatures in MSigDB.

Table S13: Results of GSEA analyses performed on ranked gene list from endpoint cells in comparison to root cells by using the hallmark gene sets (H), curated gene sets (C2), oncogenic gene sets (C6) and immunologic gene sets (C7) signatures in MSigDB.

Table S14: Signaling pathway expression scores (EGFR, Hypoxia, JAK-STAT, MAPK, NFkB, PI3K, TGFb, TNFa, Trail, VEGF, p53), inferred by PROGENy and expression signatures for NOTCH1, PIM, MYC) in single ETP-ALL cells.

Table S15: Targeted sequencing analyses of *AKT1*, *AKT2*, *NOTCH1*, *PIK3CA*, *PIK3CB*, *PIK3CD*, *PIK3R1*, *PIKR3*, *PIKR6* and *PTEN* in ETP-ALL samples, including tumor purity, average sequencing depth and coverage. Of note, patient 5 *NOTCH1* mutant allele frequency decreased with treatment. ND = not detected.

Table S16: IHC staining results for LGALS9 in ETP and T-ALL patients.

References

1. Chou TC. Theoretical basis, experimental design, and computerized simulation of synergism and antagonism in drug combination studies. *Pharmacol Rev.* 2006;58(3):621-681.
2. Bongiovanni D, Saccomani V, Piovan E. Aberrant Signaling Pathways in T-Cell Acute Lymphoblastic Leukemia. *Int J Mol Sci.* 2017;18(9).
3. Dobin A, Davis CA, Schlesinger F, et al. STAR: ultrafast universal RNA-seq aligner. *Bioinformatics.* 2013;29(1):15-21.
4. Bolger AM, Lohse M, Usadel B. Trimmomatic: a flexible trimmer for Illumina sequence data. *Bioinformatics.* 2014;30(15):2114-2120.
5. Anders S, Pyl PT, Huber W. HTSeq—a Python framework to work with high-throughput sequencing data. *Bioinformatics.* 2015;31(2):166-169.
6. Li B, Dewey CN. RSEM: accurate transcript quantification from RNA-Seq data with or without a reference genome. *BMC Bioinformatics.* 2011;12:323.
7. Fan J, Salathia N, Liu R, et al. Characterizing transcriptional heterogeneity through pathway and gene set overdispersion analysis. *Nature methods.* 2016;13(3):241-244.
8. Butler A, Hoffman P, Smibert P, Papalexi E, Satija R. Integrating single-cell transcriptomic data across different conditions, technologies, and species. *Nat Biotechnol.* 2018;36(5):411-420.
9. Lun AT, McCarthy DJ, Marioni JC. A step-by-step workflow for low-level analysis of single-cell RNA-seq data with Bioconductor. *F1000Res.* 2016;5:2122.
10. Van der Auwera GA, Carneiro MO, Hartl C, et al. From FastQ data to high confidence variant calls: the Genome Analysis Toolkit best practices pipeline. *Curr Protoc Bioinformatics.* 2013;43:11 10 11-33.
11. Cibulskis K, Lawrence MS, Carter SL, et al. Sensitive detection of somatic point mutations in impure and heterogeneous cancer samples. *Nat Biotechnol.* 2013;31(3):213-219.
12. Ramos AH, Lichtenstein L, Gupta M, et al. Oncotator: cancer variant annotation tool. *Hum Mutat.* 2015;36(4):E2423-2429.
13. Patel AP, Tirosh I, Trombetta JJ, et al. Single-cell RNA-seq highlights intratumoral heterogeneity in primary glioblastoma. *Science.* 2014;344(6190):1396-1401.
14. Tirosh I, Izar B, Prakadan SM, et al. Dissecting the multicellular ecosystem of metastatic melanoma by single-cell RNA-seq. *Science.* 2016;352(6282):189-196.
15. Muller S, Cho A, Liu SJ, Lim DA, Diaz A. CONICS integrates scRNA-seq with DNA sequencing to map gene expression to tumor sub-clones. *Bioinformatics.* 2018;34(18):3217-3219.
16. Heng TS, Painter MW, Immunological Genome Project C. The Immunological Genome Project: networks of gene expression in immune cells. *Nat Immunol.* 2008;9(10):1091-1094.
17. Fernandez JM, de la Torre V, Richardson D, et al. The BLUEPRINT Data Analysis Portal. *Cell Syst.* 2016;3(5):491-495 e495.

18. Zemmour D, Zilionis R, Kiner E, Klein AM, Mathis D, Benoist C. Single-cell gene expression reveals a landscape of regulatory T cell phenotypes shaped by the TCR. *Nature Immunology*. 2018;19(3):291.
19. Hu H, Miao YR, Jia LH, Yu QY, Zhang Q, Guo AY. AnimalTFDB 3.0: a comprehensive resource for annotation and prediction of animal transcription factors. *Nucleic Acids Res*. 2019;47(D1):D33-D38.
20. Liaw A, Wiener M. Classification and Regression by RandomForest. Vol. 23; 2001.
21. Aran D, Hu Z, Butte AJ. xCell: digitally portraying the tissue cellular heterogeneity landscape. *Genome Biol*. 2017;18(1):220.
22. Aibar S, Gonzalez-Blas CB, Moerman T, et al. SCENIC: single-cell regulatory network inference and clustering. *Nat Methods*. 2017;14(11):1083-1086.
23. Wolf FA, Angerer P, Theis FJ. SCANPY: large-scale single-cell gene expression data analysis. *Genome Biol*. 2018;19(1):15.
24. Trapnell C, Cacchiarelli D, Grimsby J, et al. The dynamics and regulators of cell fate decisions are revealed by pseudotemporal ordering of single cells. *Nat Biotechnol*. 2014;32(4):381-386.
25. La Manno G, Soldatov R, Zeisel A, et al. RNA velocity of single cells. *Nature*. 2018;560(7719):494-498.
26. Schubert M, Klinger B, Klunemann M, et al. Perturbation-response genes reveal signaling footprints in cancer gene expression. *Nat Commun*. 2018;9(1):20.
27. Boratyn GM, Thierry-Mieg J, Thierry-Mieg D, Busby B, Madden TL. Magic-BLAST, an accurate RNA-seq aligner for long and short reads. *BMC Bioinformatics*. 2019;20(1):405.
28. Chen L, Flies DB. Molecular mechanisms of T cell co-stimulation and co-inhibition. *Nat Rev Immunol*. 2013;13(4):227-242.
29. Kumar MP, Du J, Lagoudas G, et al. Analysis of Single-Cell RNA-Seq Identifies Cell-Cell Communication Associated with Tumor Characteristics. *Cell Rep*. 2018;25(6):1458-1468 e1454.
30. The results published here are in whole or part based upon data generated by the Therapeutically Applicable Research to Generate Effective Treatments (<https://ocg.cancer.gov/programs/target>) initiative, phs000218. The data used for this analysis are available at <https://portal.gdc.cancer.gov/projects>.
31. Ghandi M, Huang FW, Jané-Valbuena J, et al. Next-generation characterization of the Cancer Cell Line Encyclopedia. *Nature*. 2019;569(7757):503-508.
32. Park JE, Botting RA, Domínguez Conde C, et al. A cell atlas of human thymic development defines T cell repertoire formation. *Science*. 2020;367(6480).

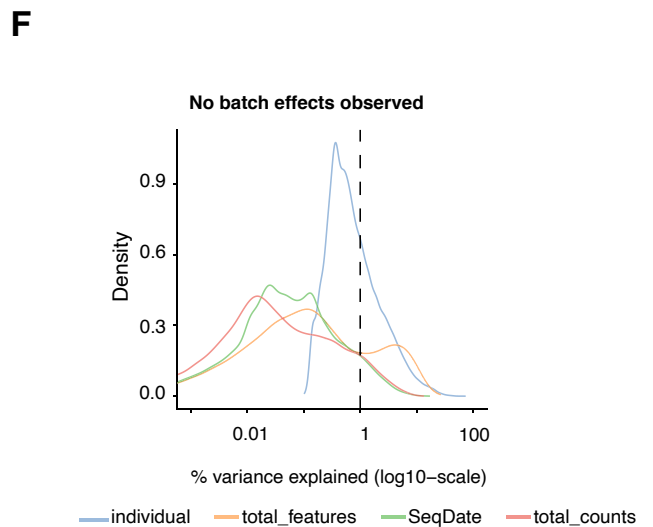
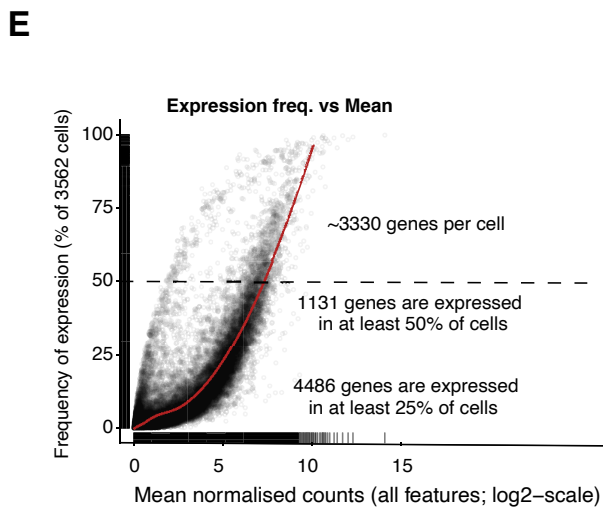
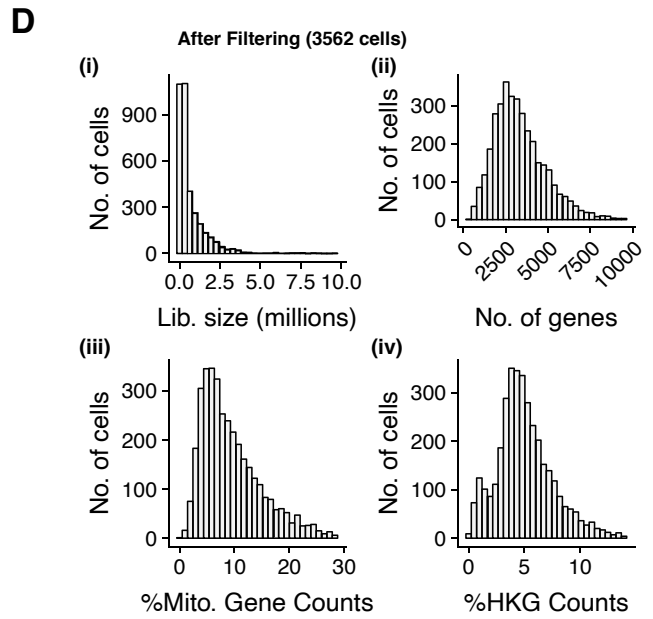
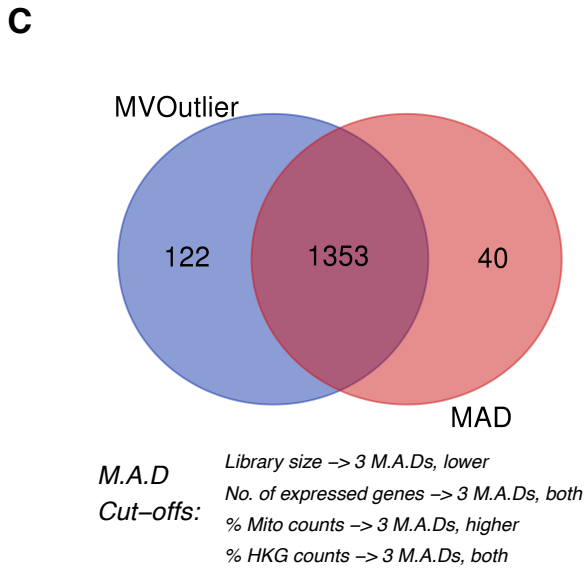
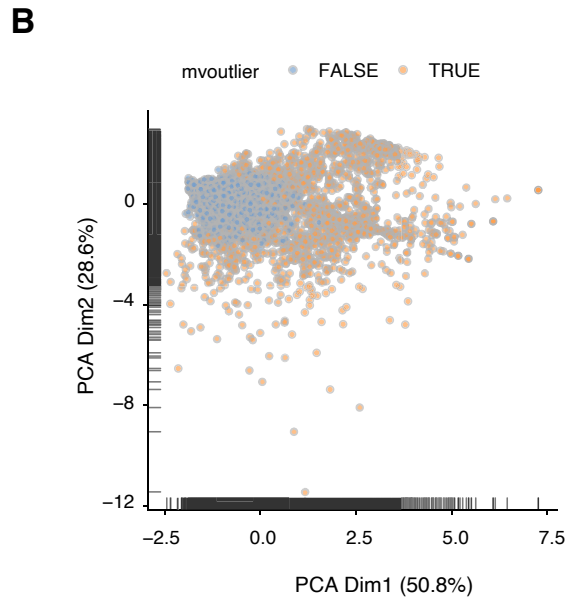
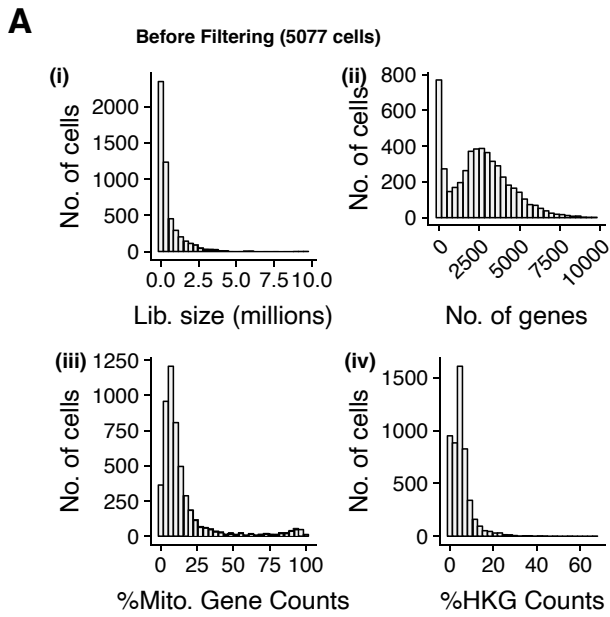


Figure S1

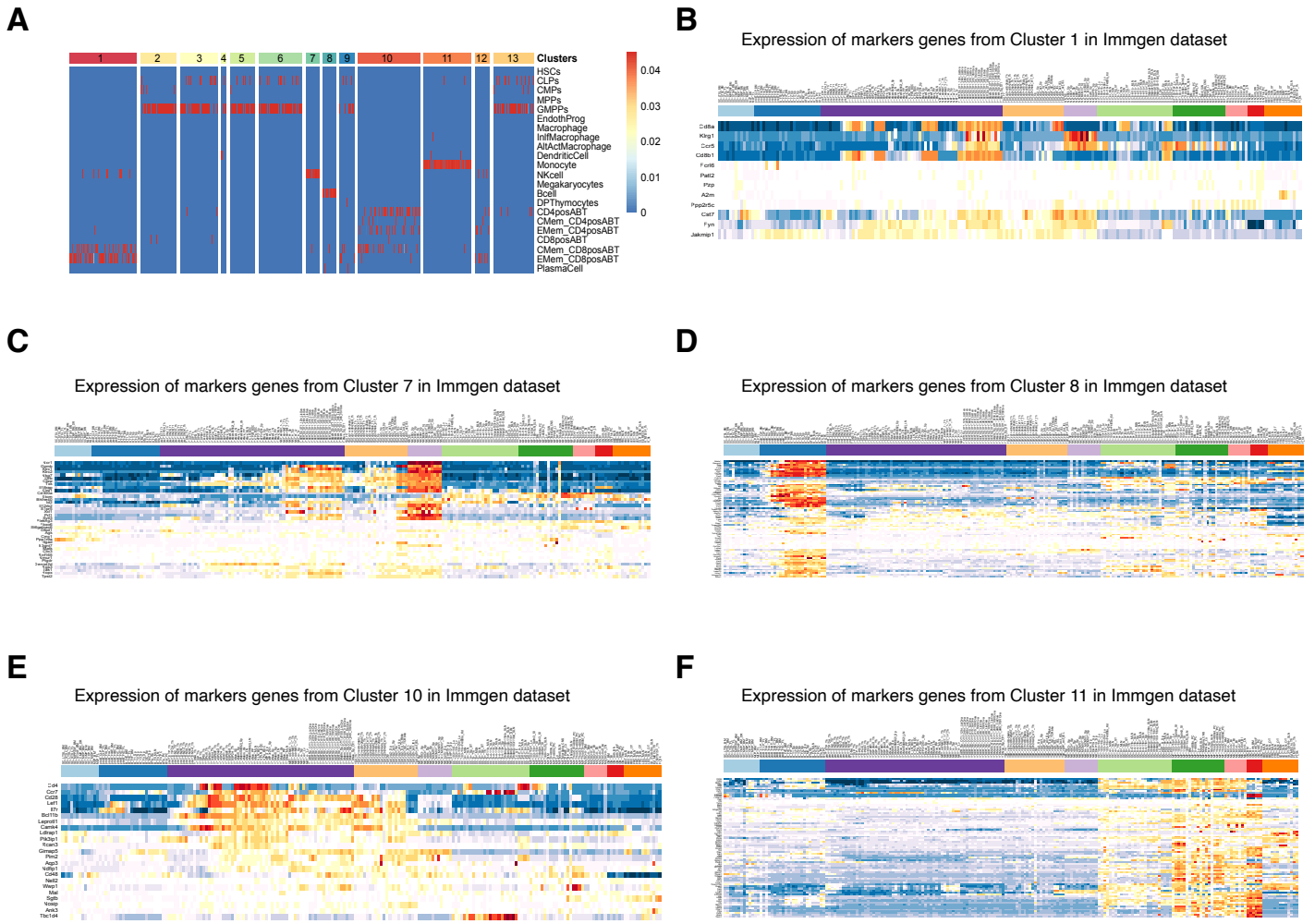


Figure S2

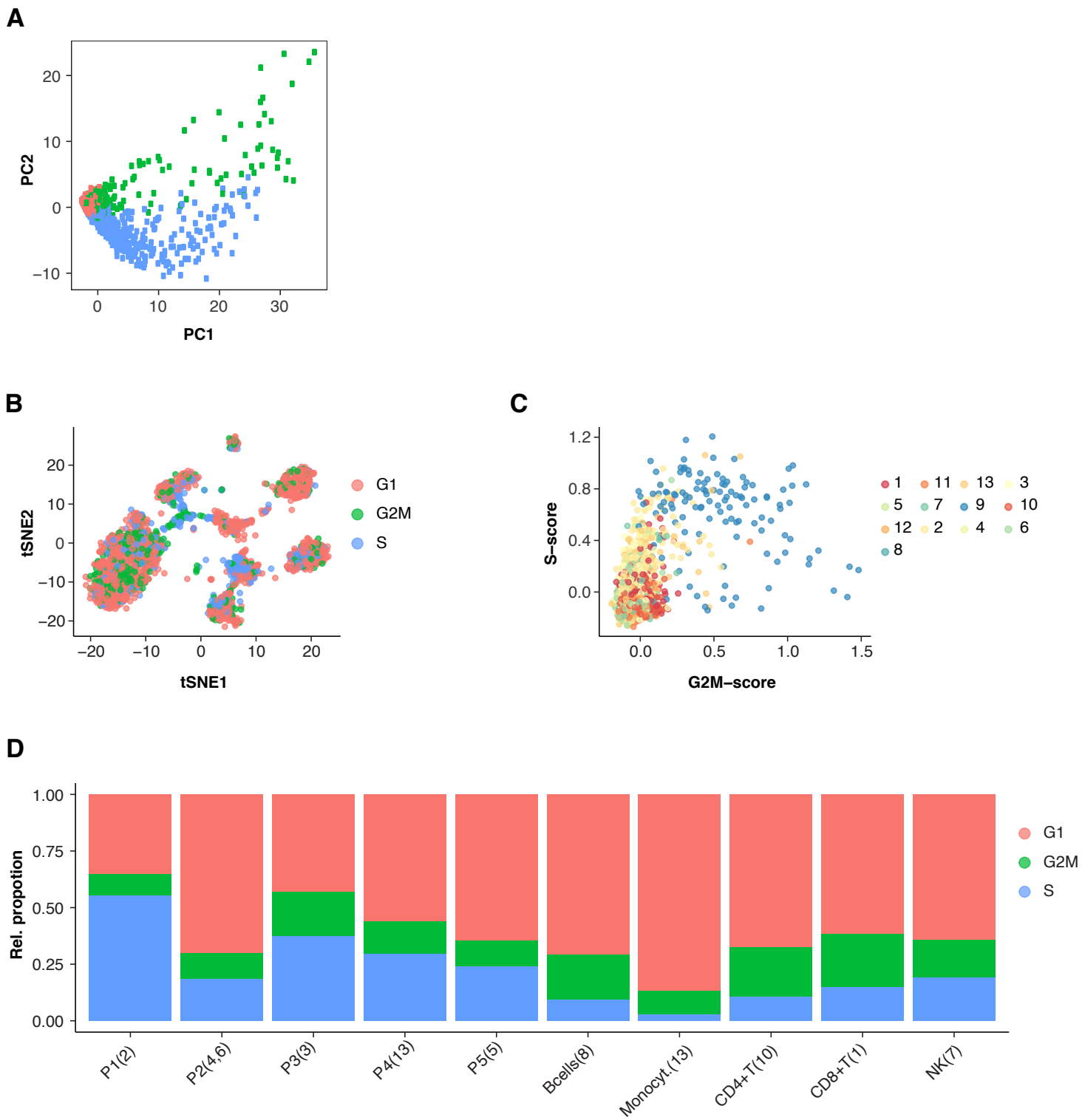


Figure S3

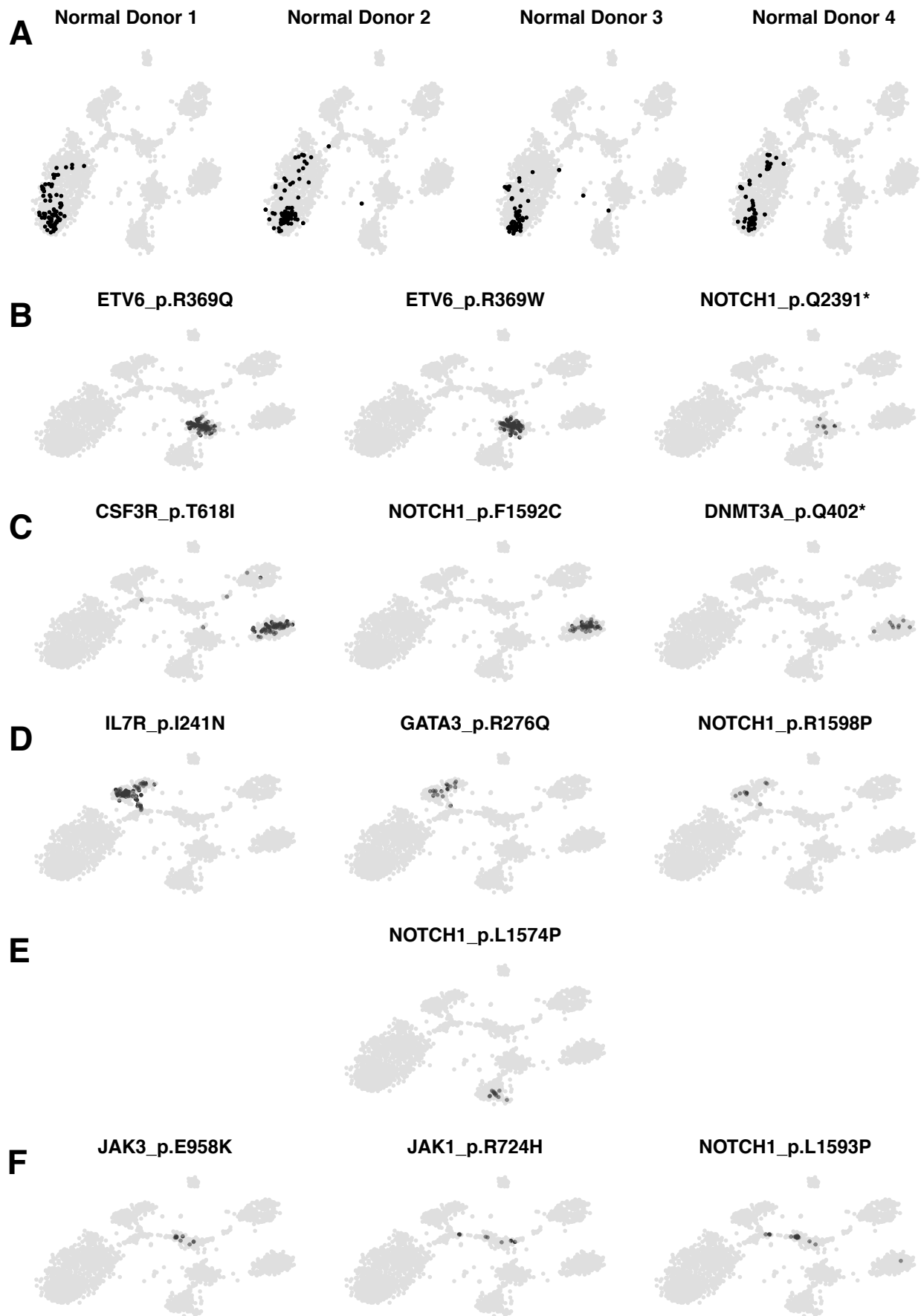
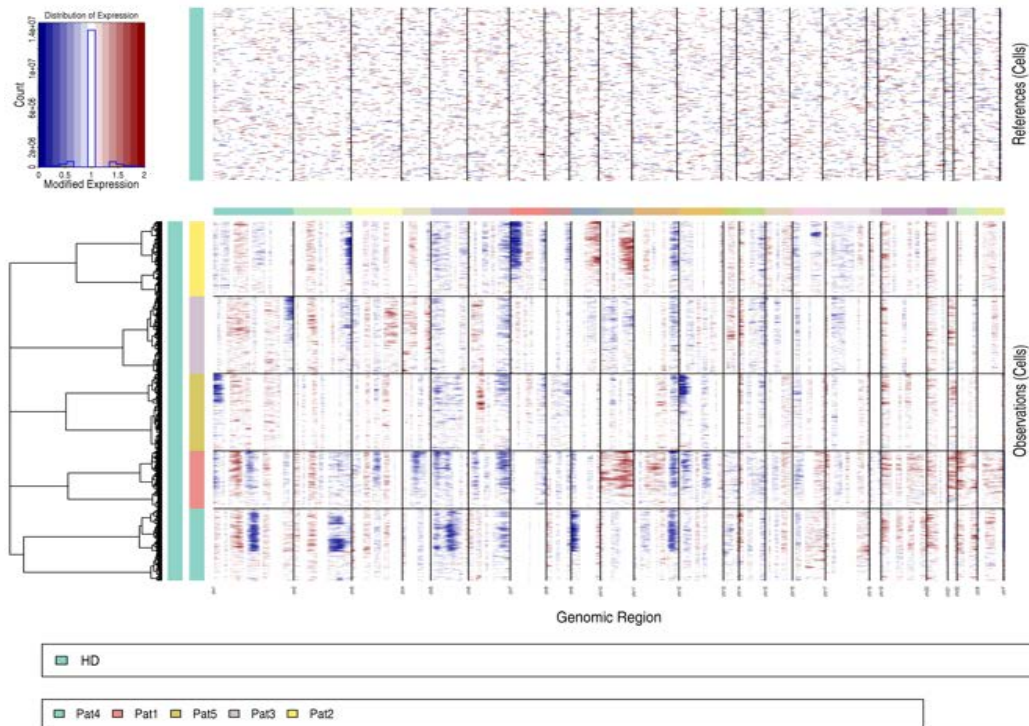
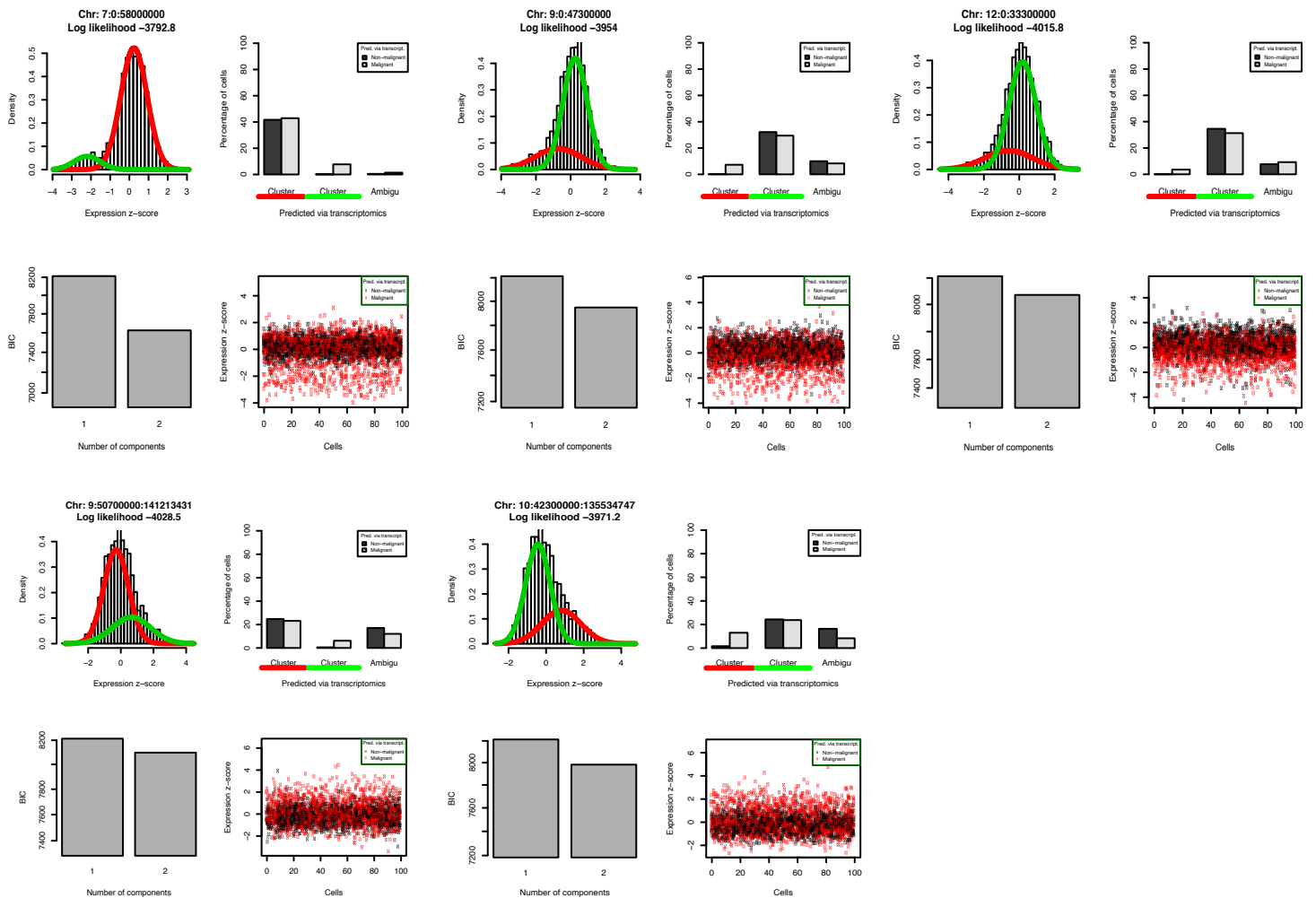


Figure S4

A

inferCNV

**B****Figure S5**

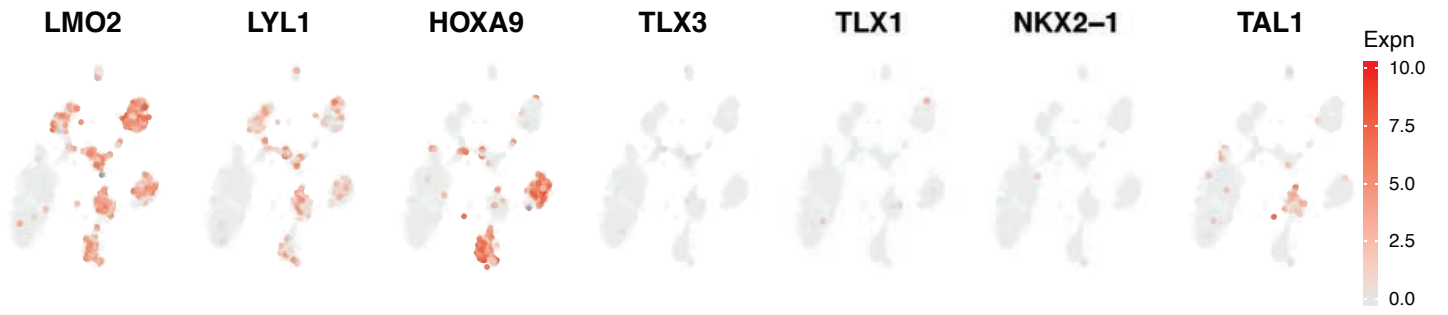


Figure S6

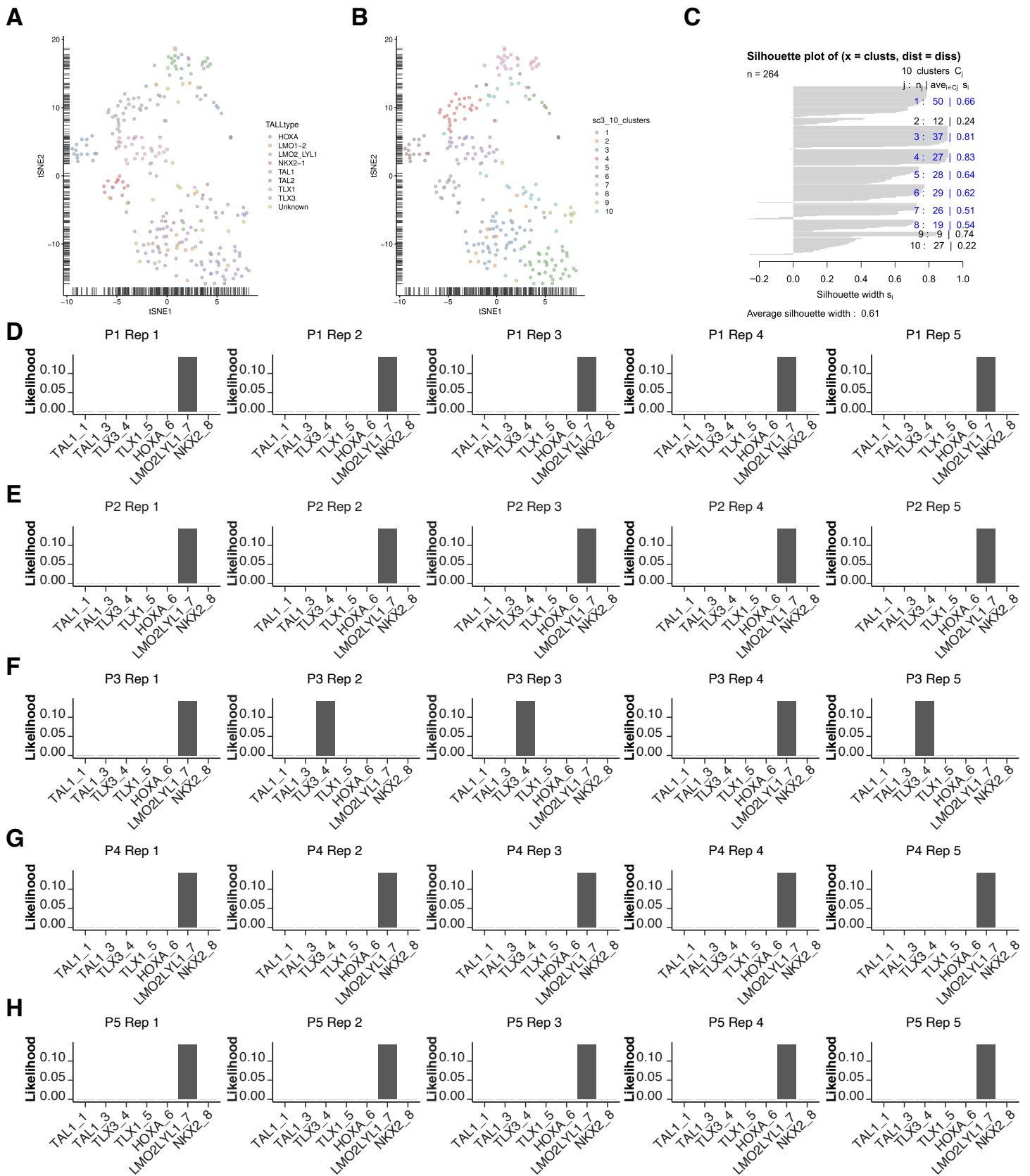


Figure S7

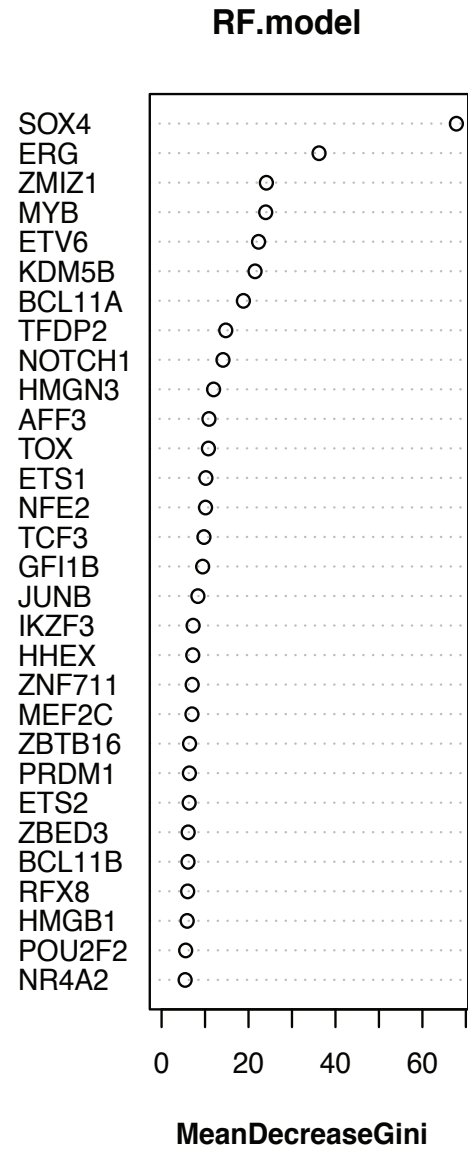
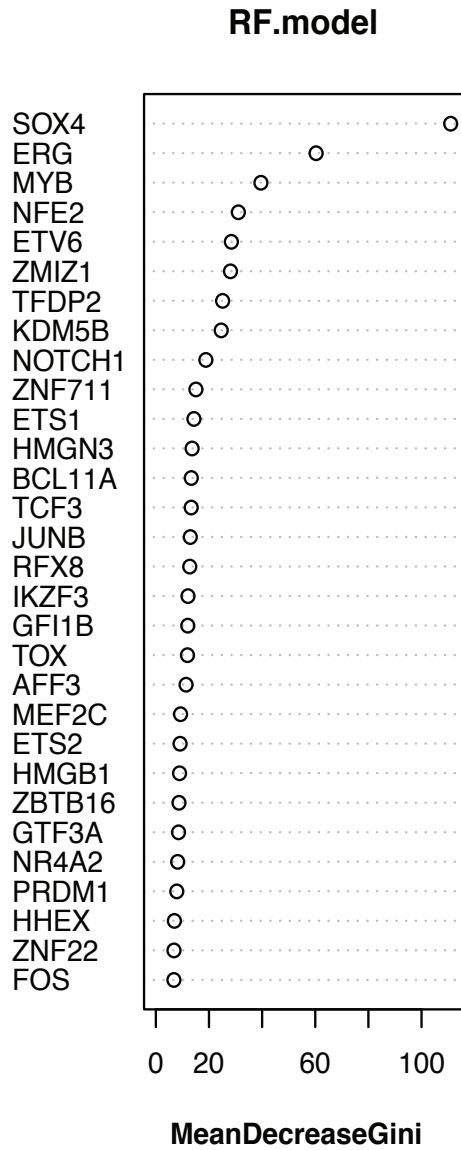
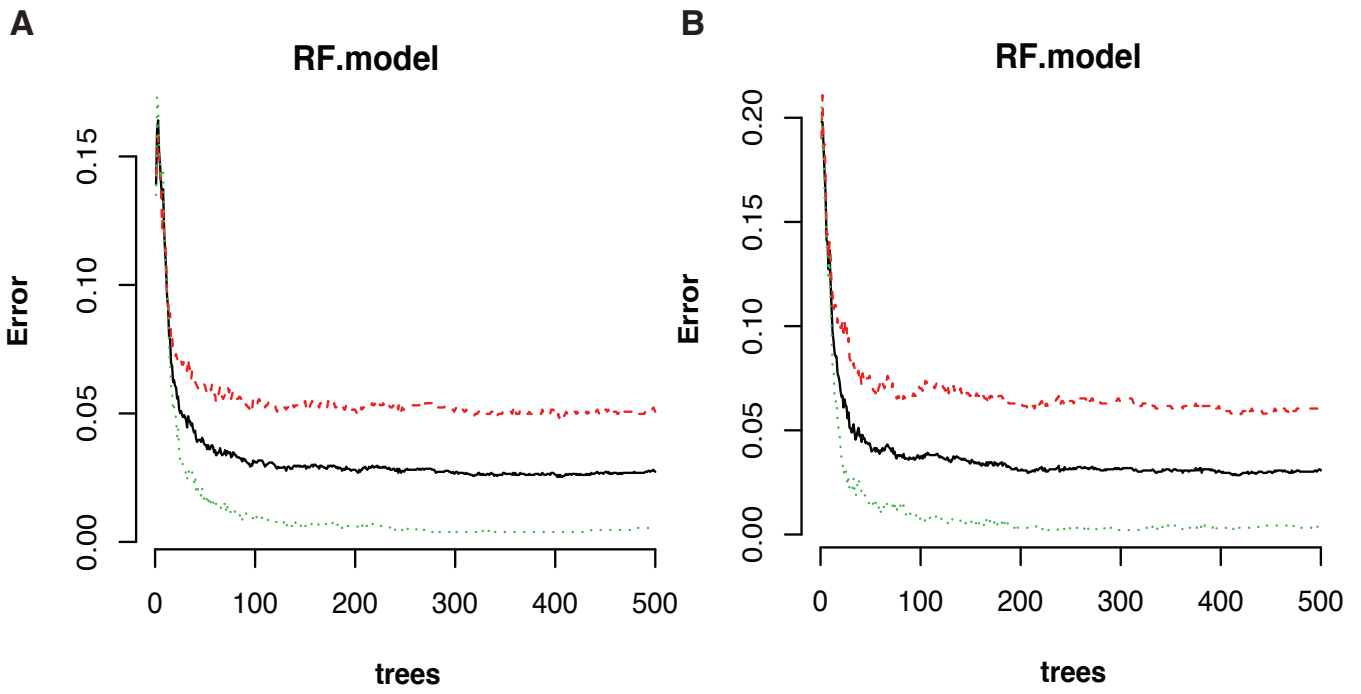


Figure S8

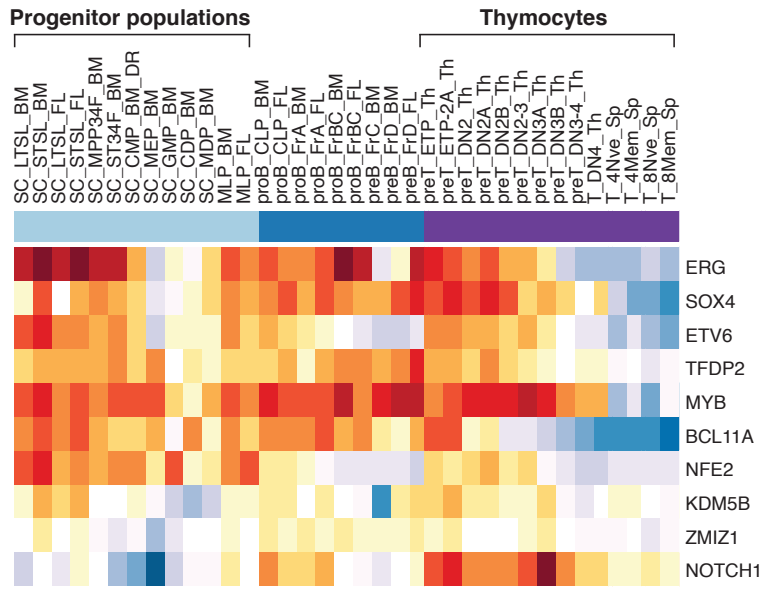
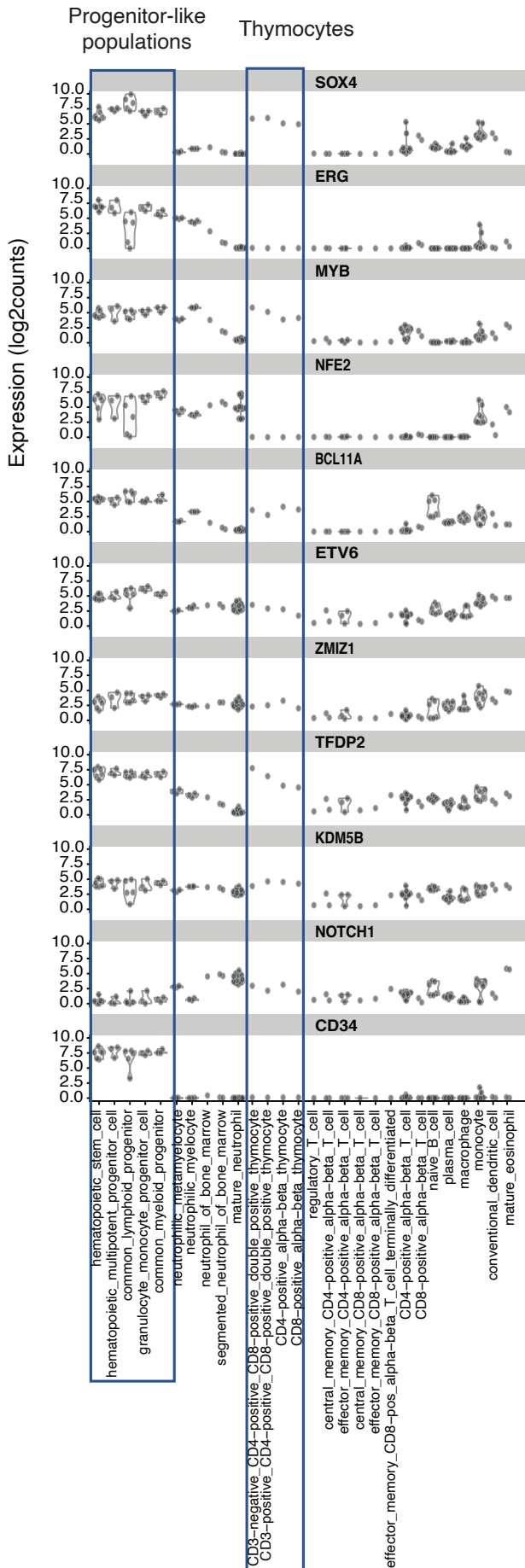
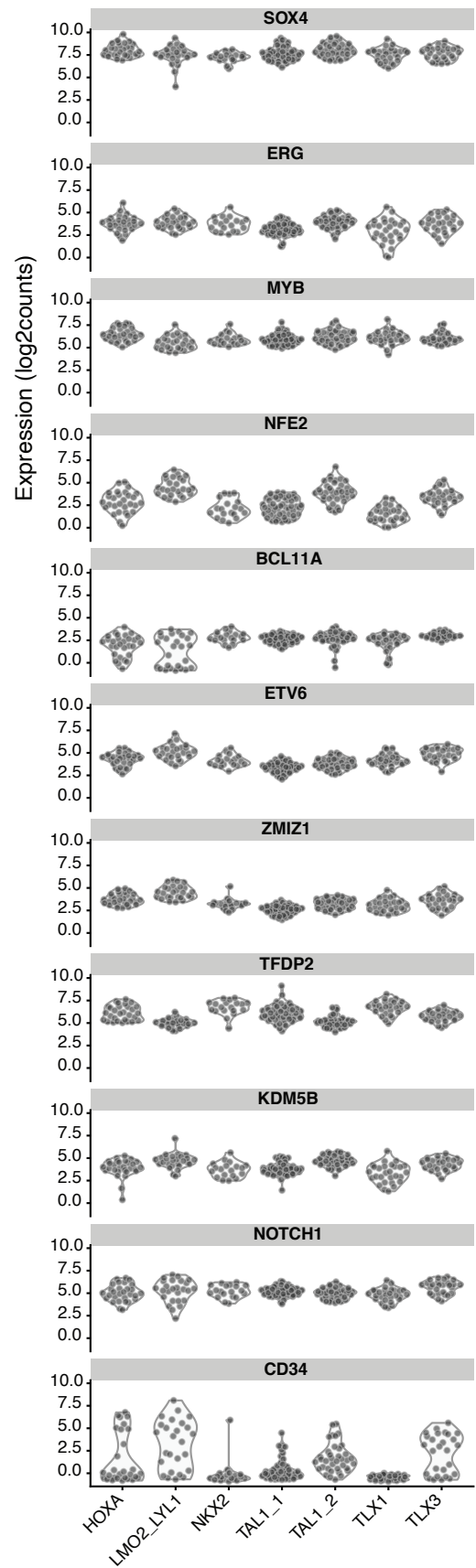
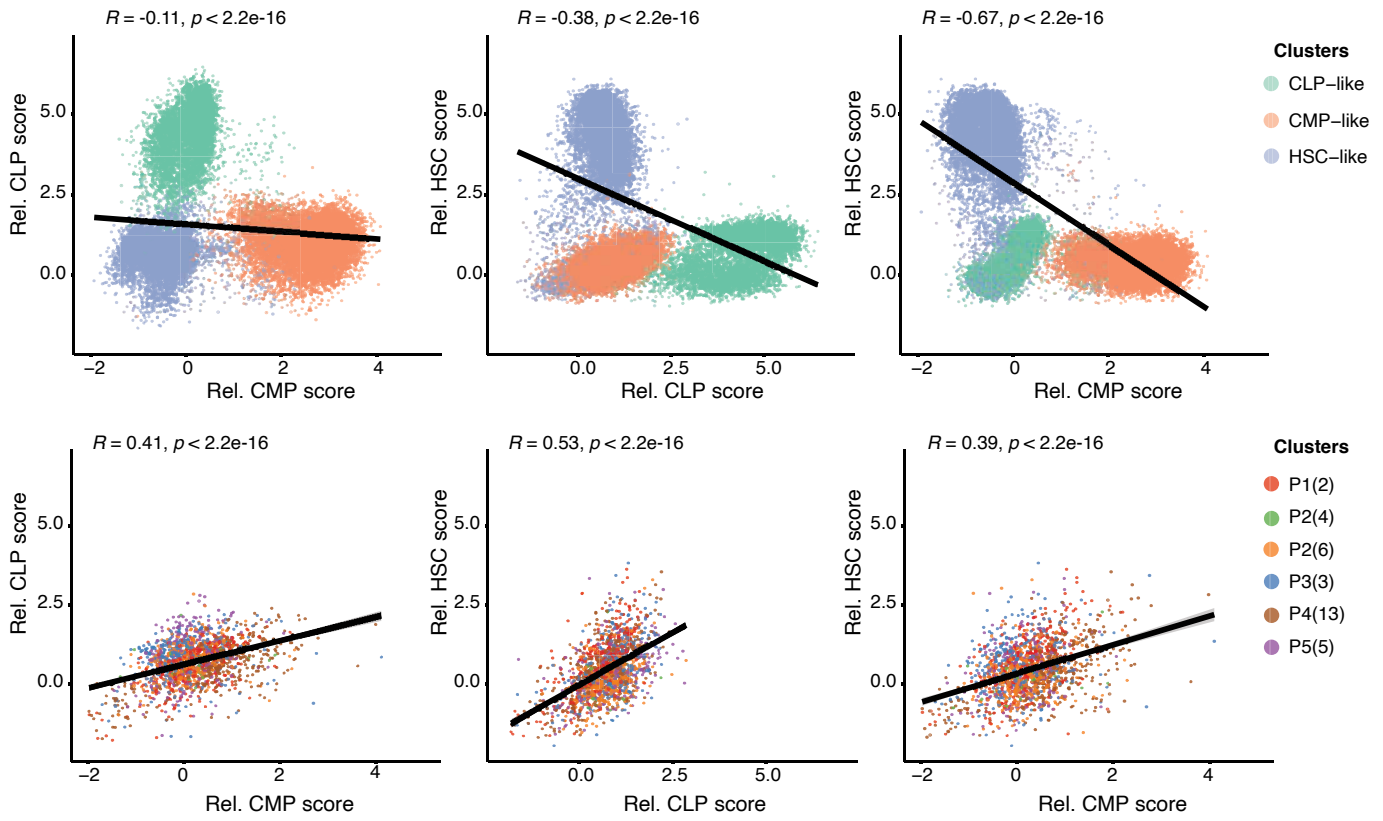
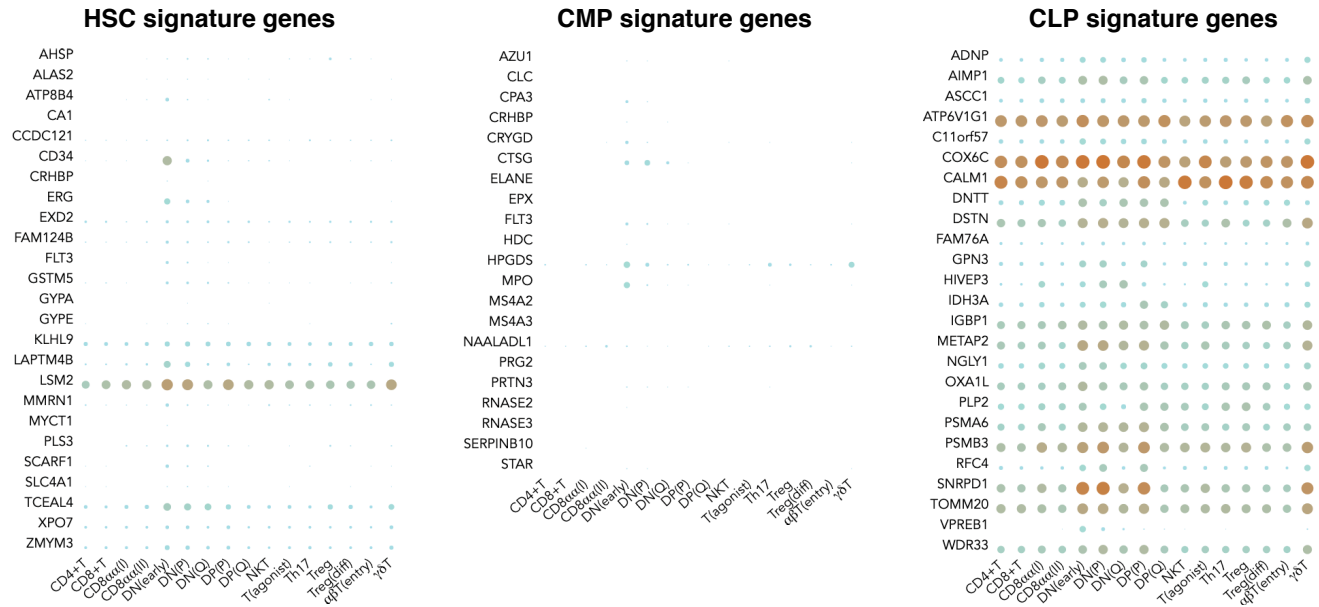


Figure S9

A**Expression of TFs in normal cells****B****Expression of TFs in T-ALL subtypes****Figure S11**

A**B****Figure S12**

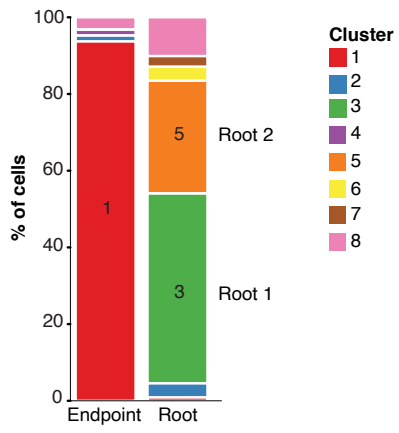


Figure S13

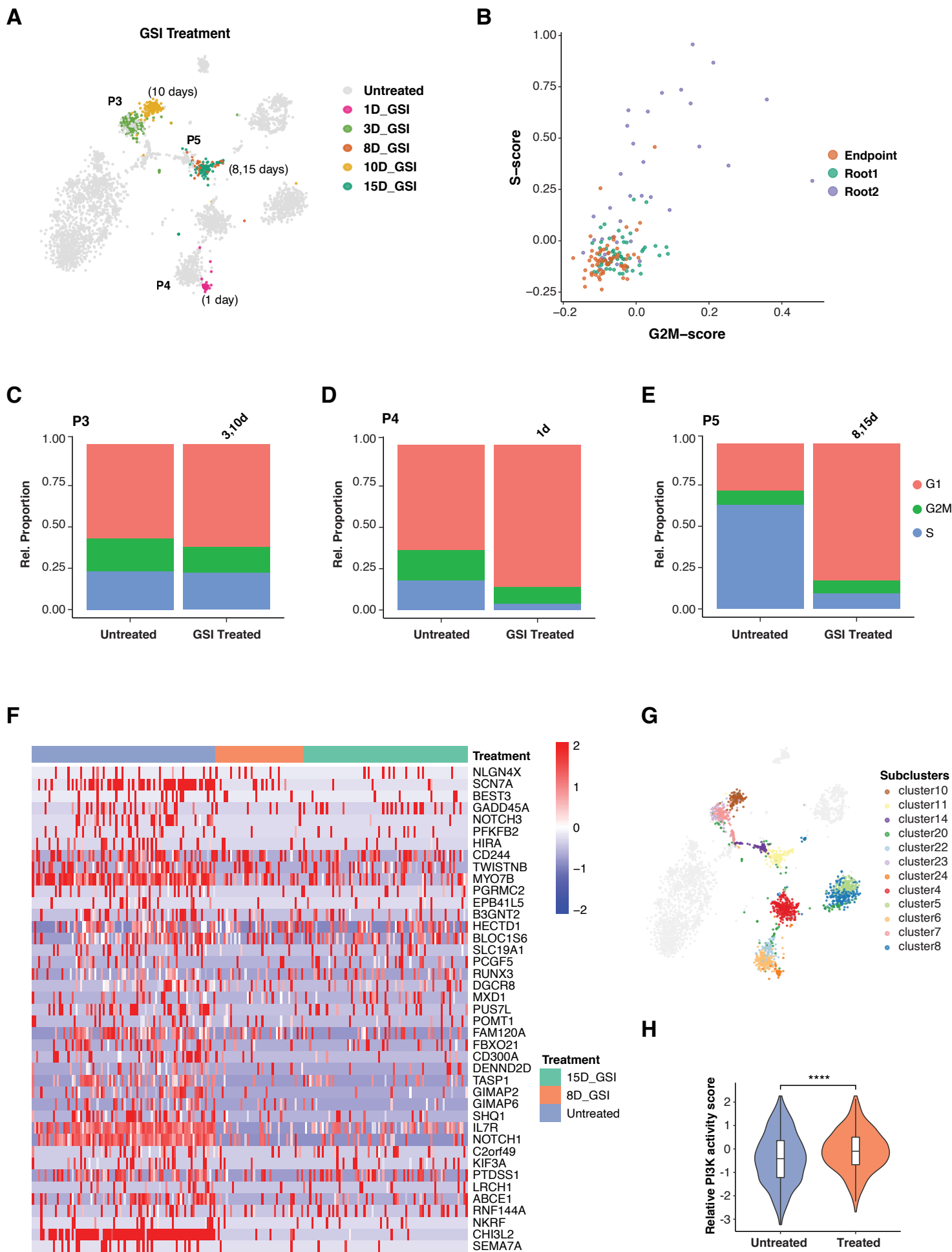


Figure S14

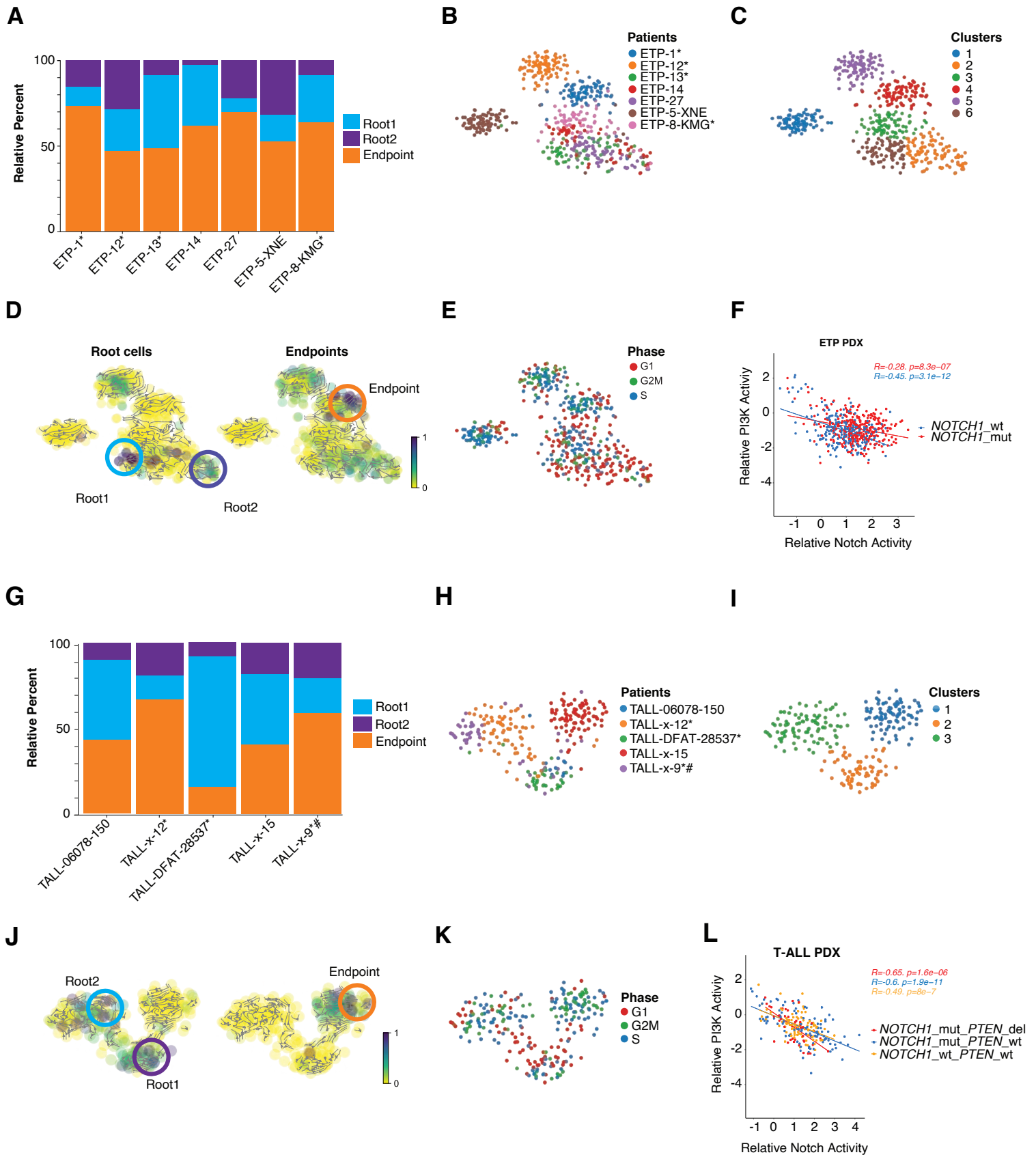
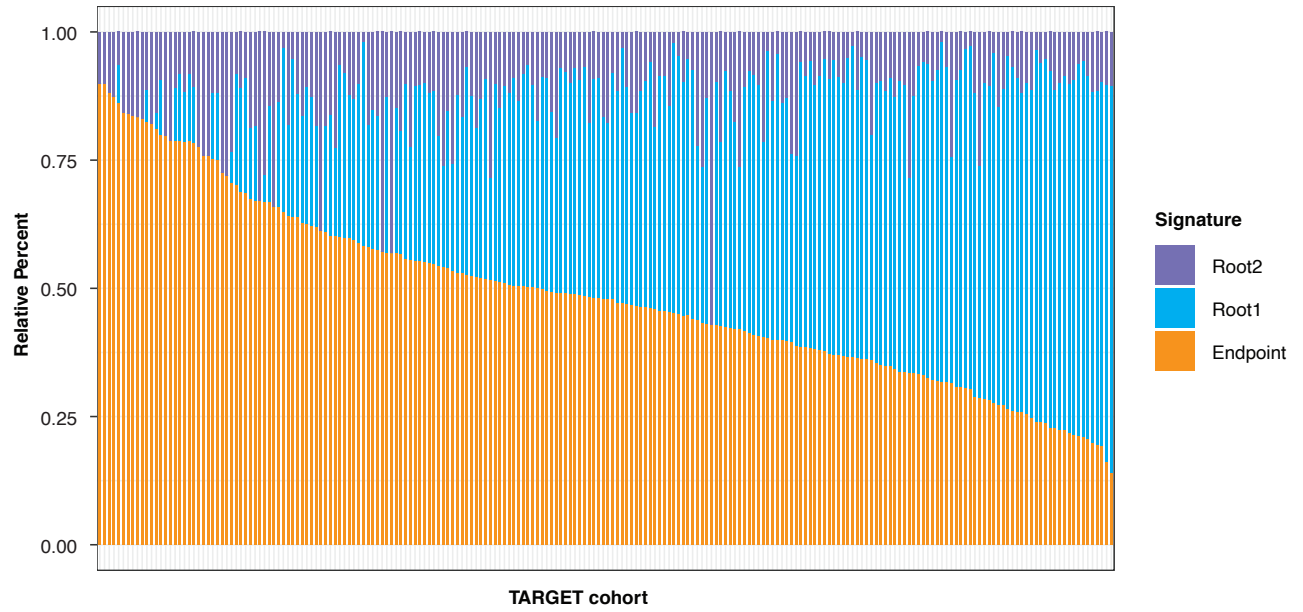
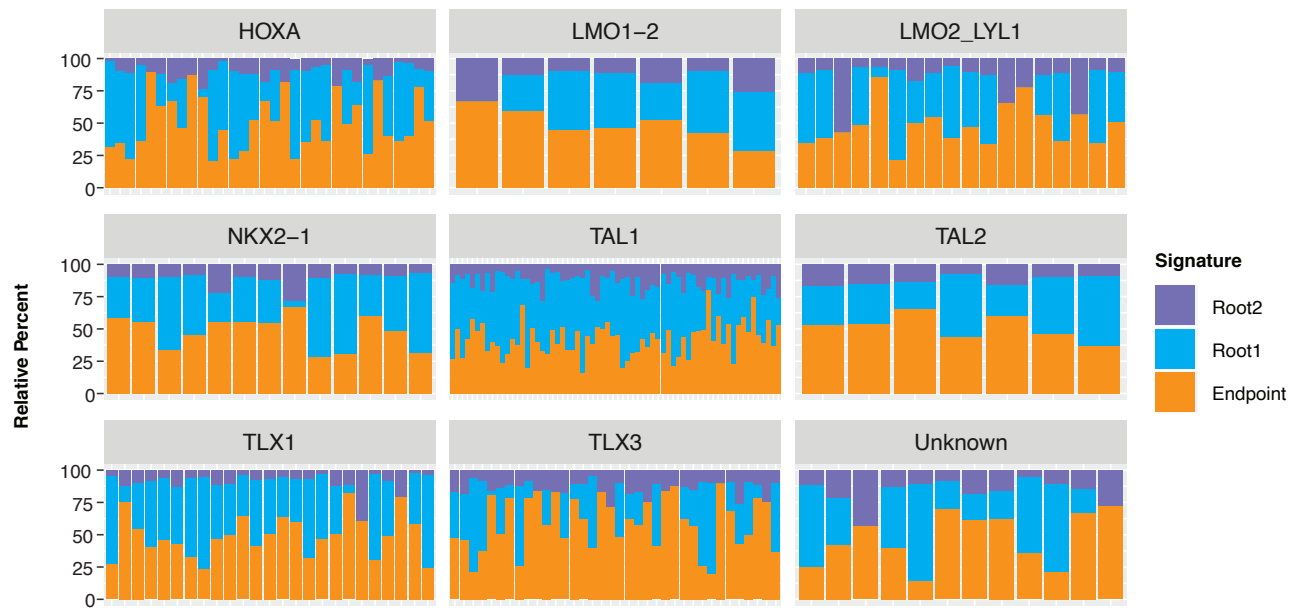


Figure S15

A**B****Figure S16**

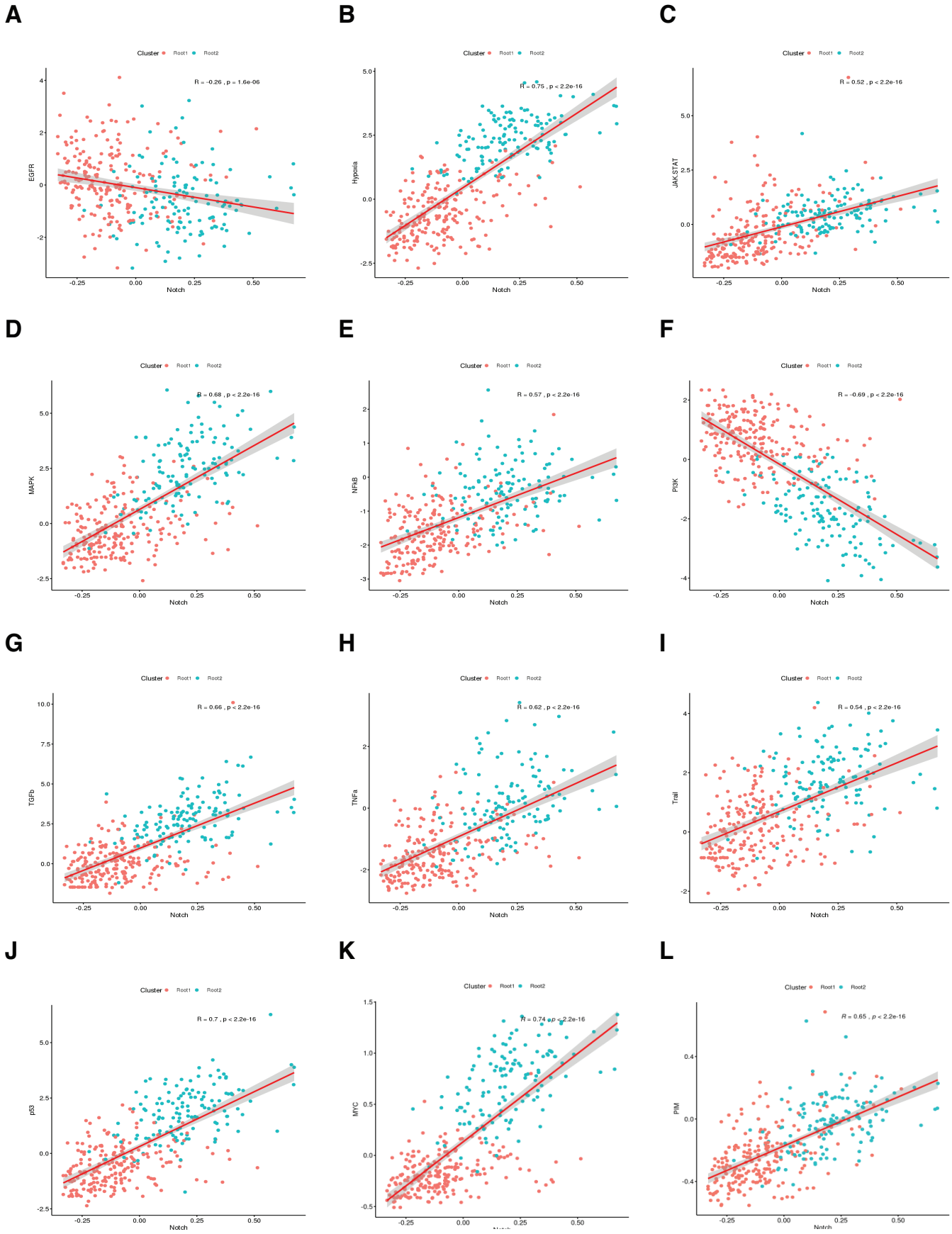


Figure S17

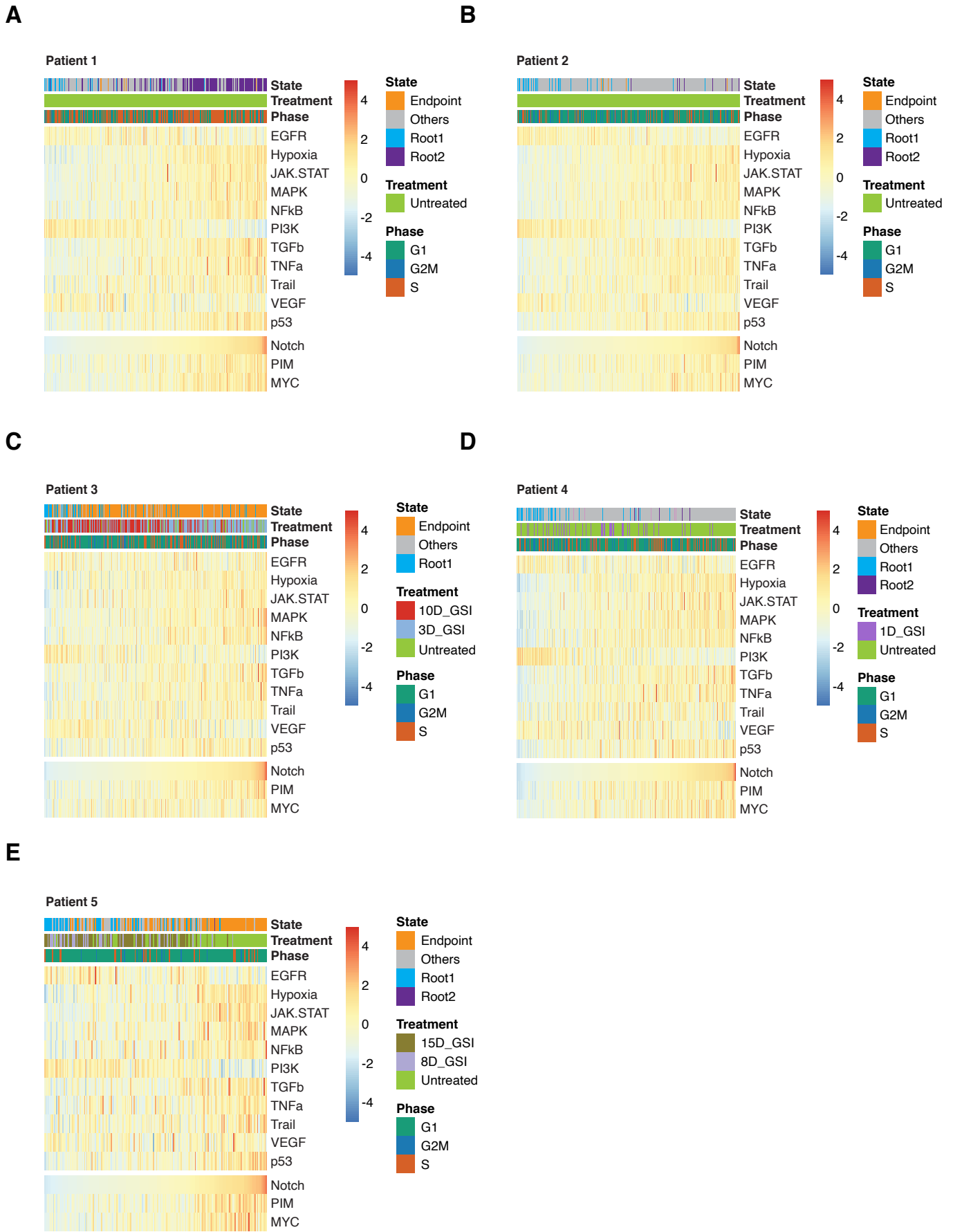
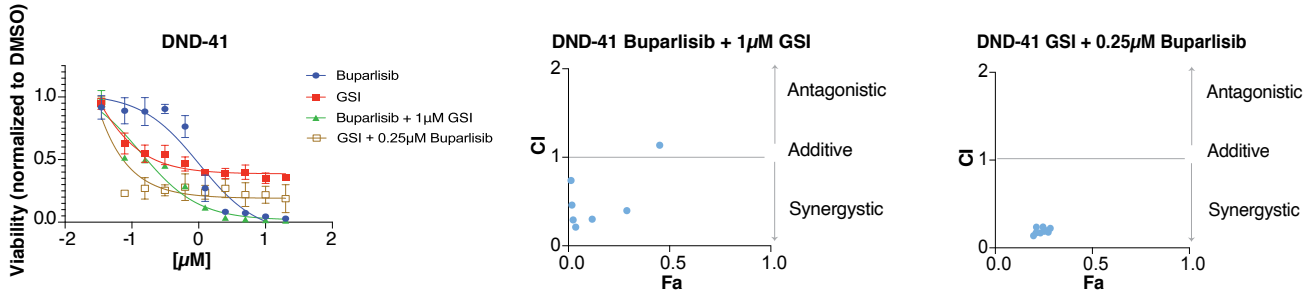
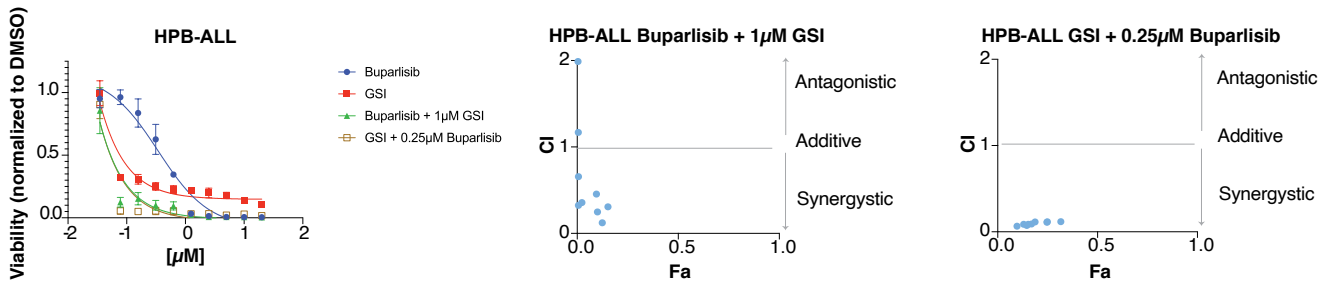
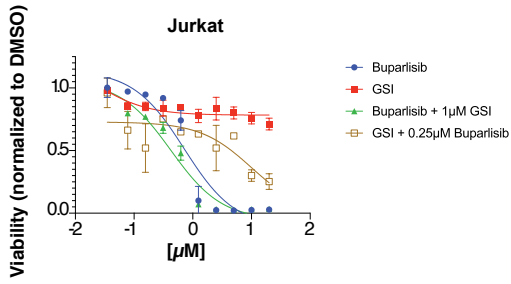
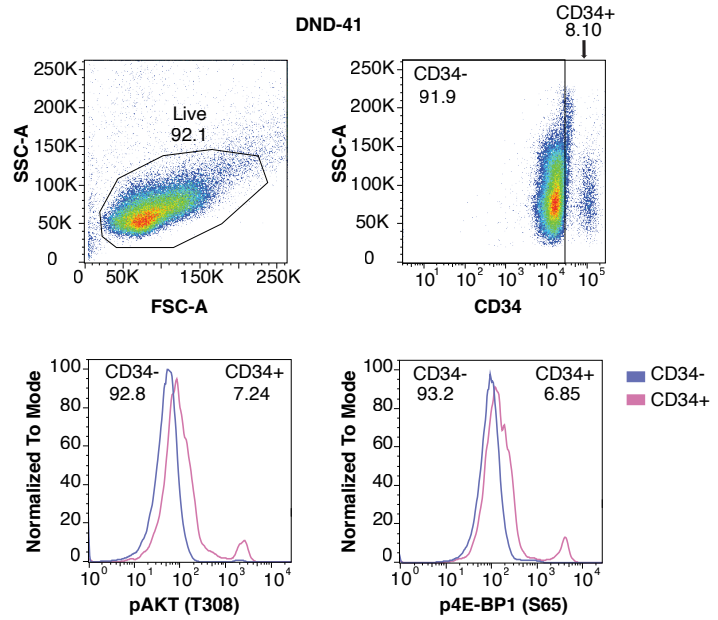
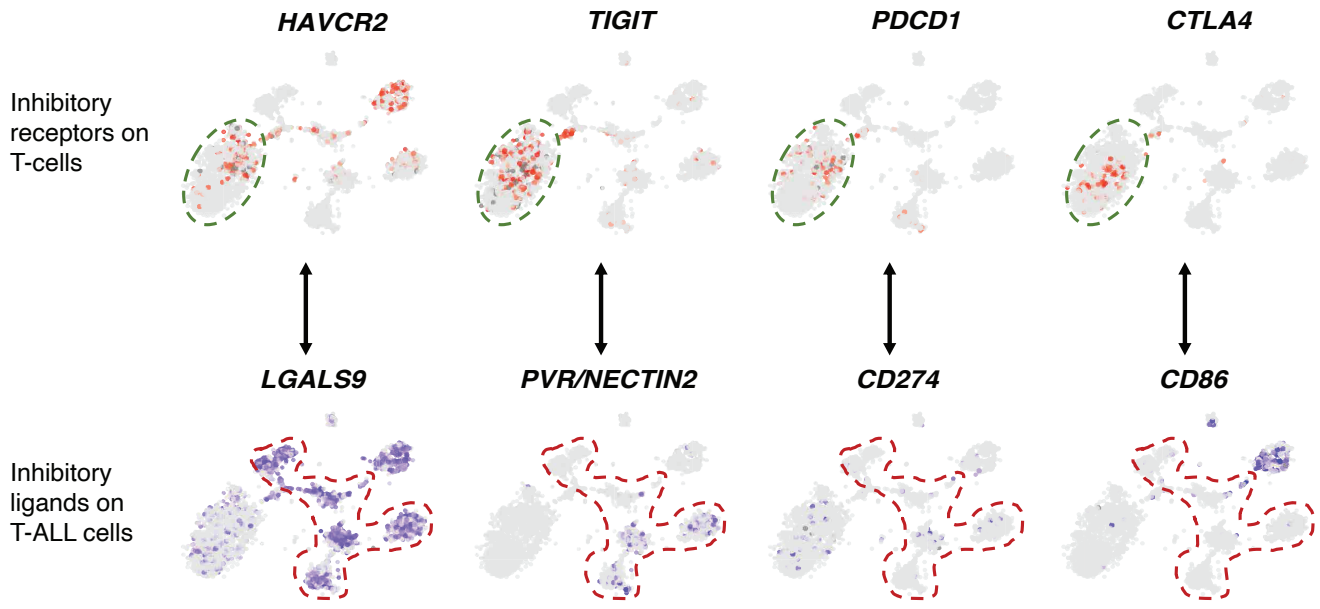
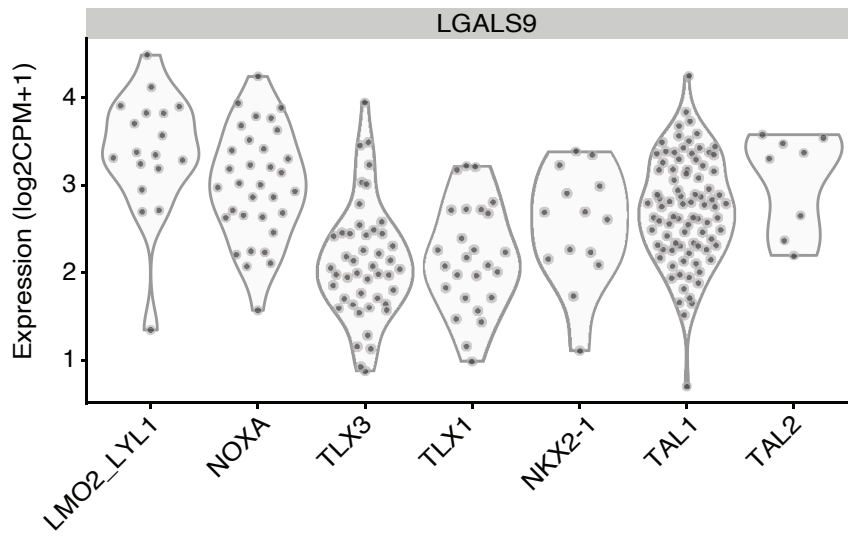
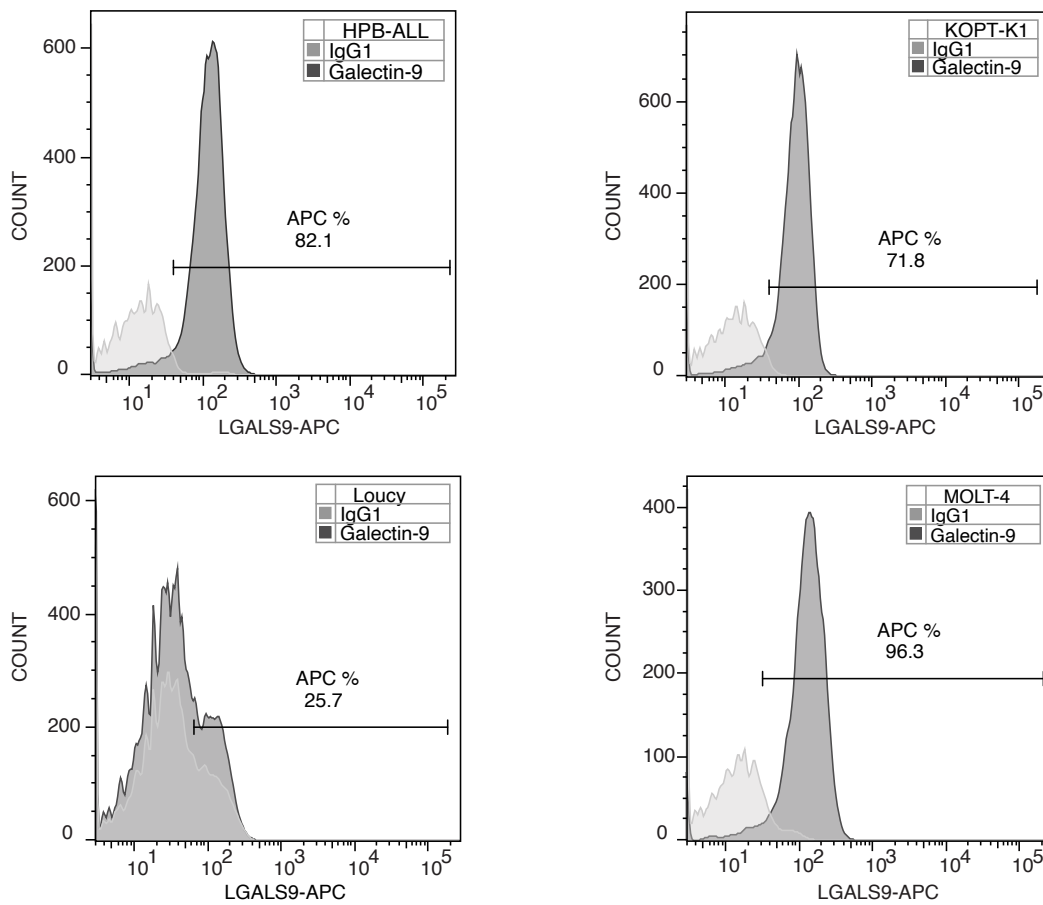
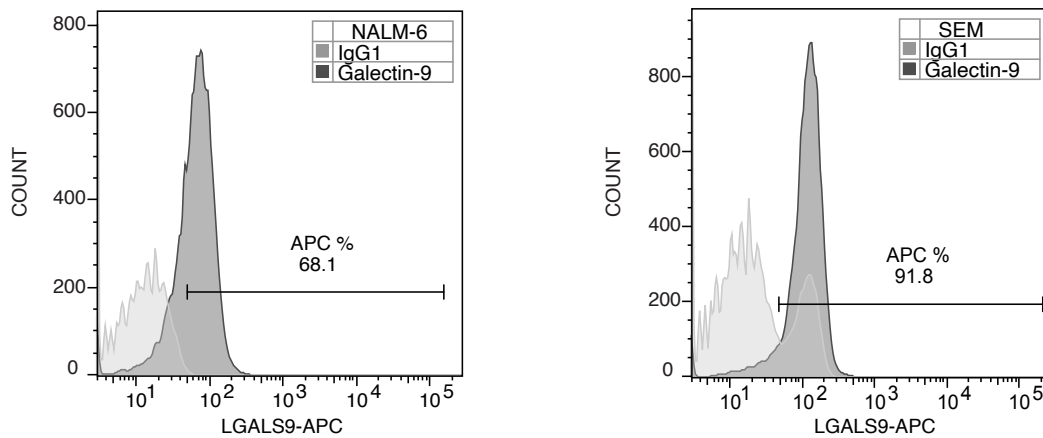
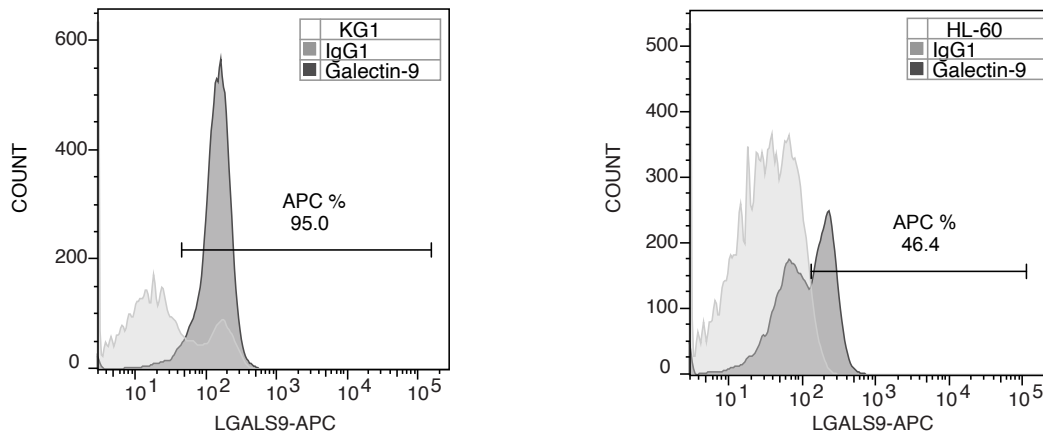


Figure S18

A**B****C****D****Figure S19**

A**B****Figure S20**

A**B****C****Figure S21**

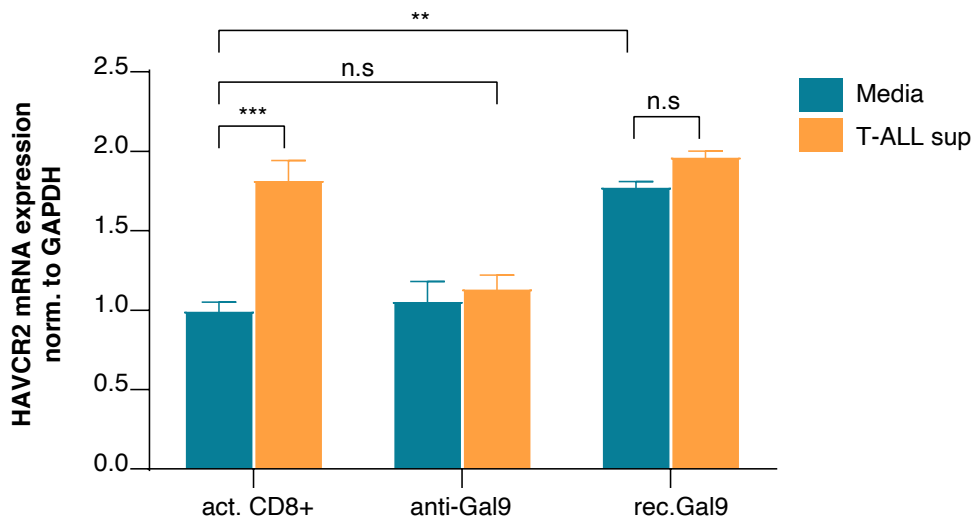


Figure S22

Flow sorting strategy for leukemia blasts

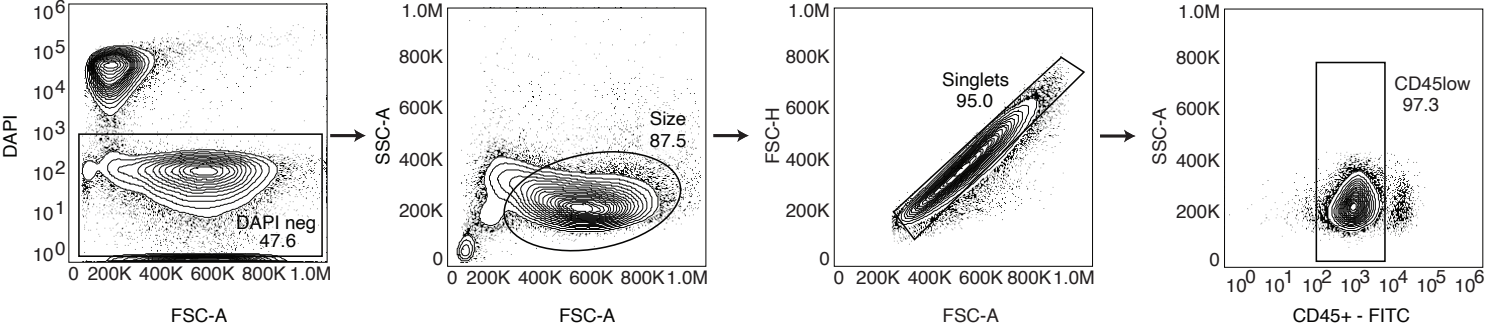


Figure S23

Flow sorting strategy for CD19+ B-cells, CD3+ T-cells and CD14+ monocytes

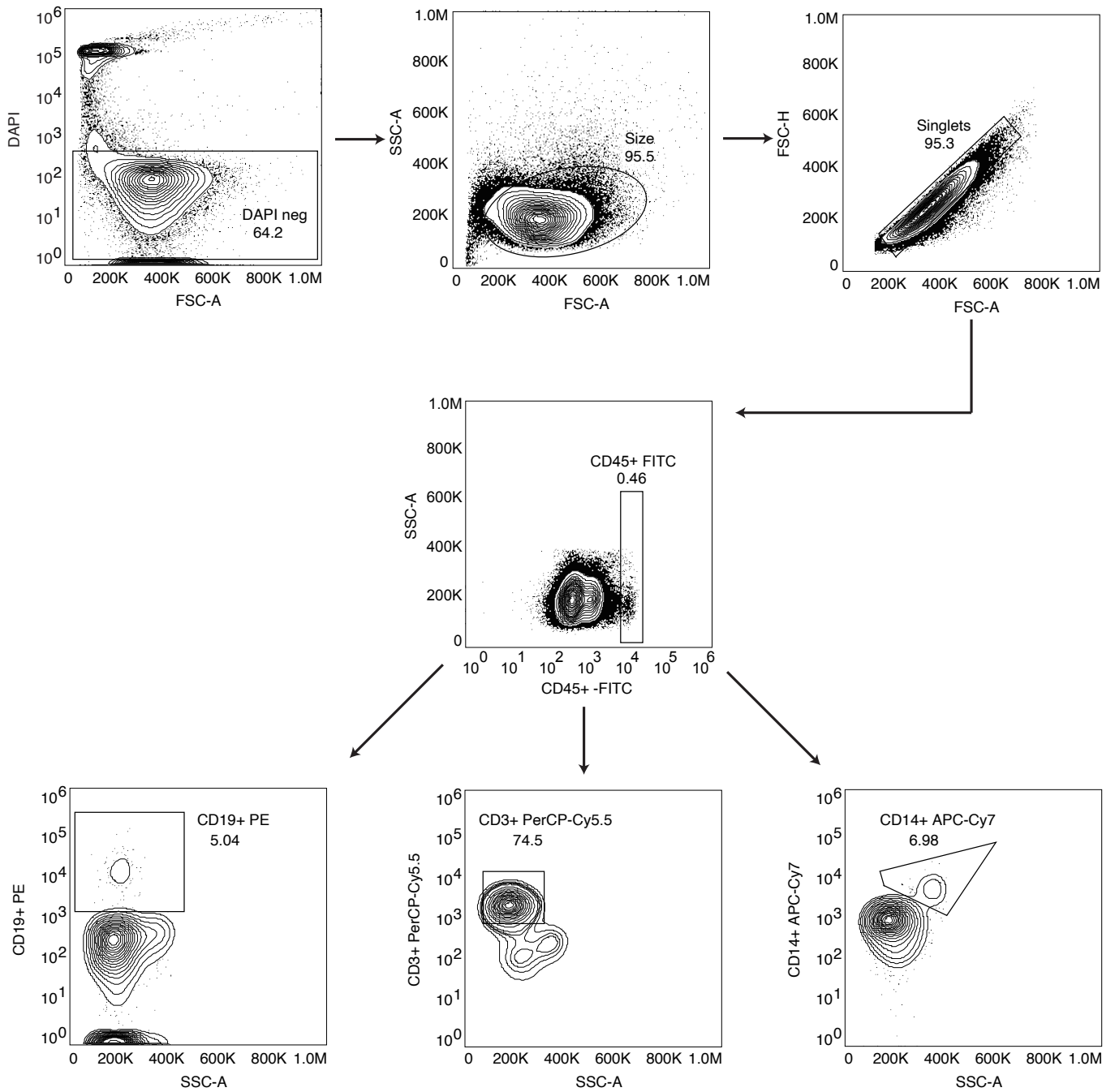


Figure S24